ENGINEERING

A reconfigurable dielectric elastomer actuator via phase-transitional ferrofluid enables sustainable operation

Yun Hyeok Lee[1]†, Seung Won Moon[1]†, Min-Gyu Lee[1]†, Won Jun Song[1], Seong-Yu Choi[1], Gimin Sung[1], Yong Eun Cho[1], Junhyun Choi[1], Byung Ik Park[1], Younghoon Lee[2], Ho-Young Kim[3,4]*, Jeong-Yun Sun[1,4,5]*

Dielectric elastomer actuators (DEAs) are promising soft transducers capable of rapid and precise actuation. However, their conventional architecture for efficient actuation confines DEAs in predesigned operational modes, leading to limited applications. Here, we introduce a reconfigurable DEA system using phase-transitional ferrofluid (PTF) electrodes. PTF switches its states between solid and liquid, satisfying requirements for a reconfigurable electrode for DEAs. In the sol state, the stable and high magnetic responsiveness inspired by ferrofluid and the low viscosity achieved through plasticization collectively enable dynamic reconfiguration of the electrode. In the gel state, PTF ensures stable shape retention and exhibits reduced interfacial slip during DEA actuation. This reconfigurable nature greatly increases adaptability and ensures continuous operation even when electrodes undergo disconnection or dielectric failure. Moreover, the PTF electrodes can be retrieved and reused after actuation, demonstrating their excellent recyclability. The combination of mechanical compliance, magnetic reconfigurability, and material sustainability renders the PTF a versatile electrode strategy for next-generation reconfigurable electroactive systems.

INTRODUCTION

Soft robots, owing to their inherent softness, can generate versatile actuation for flexible adaptation to unstructured environments and purposes (*1*–*4*). This adaptability of soft robotic systems is advantageous for emulating the efficiency and high degrees of freedom observed in human muscles (*5*–*7*). Among various soft transducers, dielectric elastomer actuators (DEAs) are considered highly promising for realizing artificial muscles because of their precise motion control under electric fields, rapid response, and high power density (*8*–*17*).

To achieve fast and efficient actuation, DEA systems have relied on long-standing architectures, such as prestretched frameworks and sandwich structures (*18*). However, this approach constrained the DEA design space and thus necessitated the fabrication of separate designs to achieve different actuation modes, unlike biological muscles that can perform complex behaviors within a single structure. In response to these limitations, there have been important attempts to broaden the flexibility of actuation including multilayered architectures (*19*–*22*), localized stiffness modulation (*23*), and the interconnection of multiple DEA modules (*24*). Although these strategies demonstrate diverse mechanical motions, they still share common challenges: Their predesigned electrodes remain permanently patterned and immobile, restricting seamless reconfiguration in a single device. Beyond merely operating within fixed electrode designs, higher actuation flexibility can be realized across diverse operating conditions when the location and geometry of electrodes are dynamically reconfigurable.

The dynamically reconfigurable electrodes need to incorporate two key operational modes. First, in the actuation mode, the electrode should exhibit solid-like behavior to effectively transmit the Maxwell stress. It should be sufficiently soft to accommodate large deformations (*25*) while maintaining structural stability and elasticity to ensure durable actuation. Second, in the modifying mode, the electrode requires fluid-like behavior to enable dynamic reconfiguration under external stimuli. The electrode should be highly responsive to external forces and have low viscosity so as not to resist bulk movement. We believe that a phase-transitional material combined with magnetoresponsive properties can simultaneously satisfy both requirements even within conventional structures, providing a previously unexplored design of reconfigurable DEA (rDEA) systems.

Here, we introduce a highly reconfigurable DEA platform enabled by a phase-transitional ferrofluid (PTF) electrode capable of freely switching between the gel state and the sol state. In the gel state, an ethylene glycol (EG)–based gelatin matrix can remain soft and elastic while maintaining high thermal stability, thereby allowing stable and large areal strain across a variety of dielectric substrates. In the sol state, liganded magnetic nanoparticles (MNPs) exhibit stable dispersion and collective motion under a magnetic field, facilitating dynamic reconfiguration of the electrode. By exploiting this reversible phase transition, we aim to reconfigure the location, number, and shape of actuation within a single device, thereby imparting design flexibility to DEAs. Moreover, the reconfigurable electrode enhances the sustainability of DEA even under dielectric or electrode failure and their recyclability over multiple cycles. Beyond DEAs, this adaptive electrode design can be extended to broader electroactive systems, ultimately advancing toward the adaptive and versatile functionalities of artificial muscles.

[1]Department of Materials Science and Engineering, Seoul National University, Seoul 08826, South Korea. [2]Department of Mechanical Engineering, Kyung Hee University, Yongin, Gyeonggi 17104, Republic of Korea. [3]Department of Mechanical Engineering, Seoul National University, Seoul 08826, South Korea. [4]SNU Energy Initiative, Seoul National University, Seoul, Republic of Korea. [5]Research Institute of Advanced Materials (RIAM), Seoul National University, 1 Gwanak-ro, Gwanak-gu, Seoul 08826, South Korea.
*Corresponding author. Email: hyk@snu.ac.kr (H.-Y.K.); jysun@snu.ac.kr (J.-Y.S.)
†These authors contributed equally to this work.

RESULTS

Designing PTF for an rDEA

The rDEA can perform multiple actuation modes by electrode reconfiguration, rather than a single, predesigned motion (Fig. 1A). We designed a reconfigurable electrode capable of manipulating the electric field at desired locations and in specific shapes. To enable such reconfiguration, the rDEA electrode should have not only solid-like properties for actuation but also fluid-like properties. However, meeting these dual requirements raises a fundamental material challenge. A robust elastic response demands a strongly connected network that transmits, stores, and recovers mechanical energy. Yet, the strong intermolecular interactions that provide this integrity also hinder segmental mobility, thereby greatly reducing the fluidic response. To overcome these conflicting material requirements, we use a phase-transitional network in which polymer chains can reversibly associate and uncoil, providing elastic support during actuation and fluidic mobility during reconfiguration. In addition, the magnetic field was chosen as the external stimulus for reconfiguration because of its unique advantages: It offers precise spatial and temporal programmability and enables wireless, noncontact

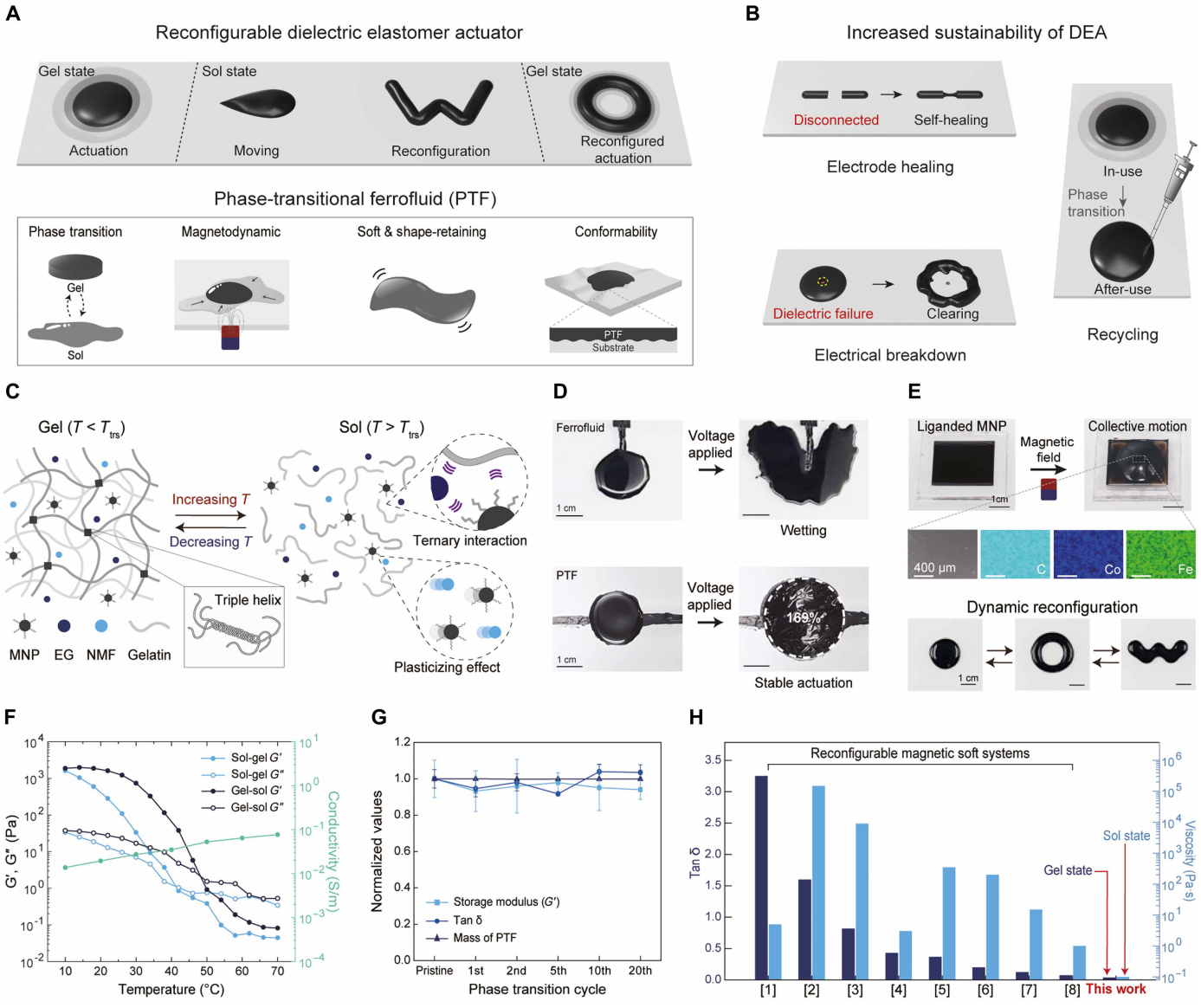

Fig. 1. Designing PTF for an rDEA. (**A**) Schematic of an rDEA and physical properties of PTF used as the electrode of DEA. (**B**) Schematic of increasing the sustainability of DEAs. Electrode healing, dielectric failure recovery, and recycling can be achieved using PTF. (**C**) Schematic diagram of PTF design. The ternary interaction among the solvent, MNPs, and gelatin should be considered to achieve a magnetic response. In addition, the plasticizing effect is needed to ensure fluidity in the sol state. (**D**) Comparison of actuation behavior with and without a phase transition. PTF enables stable actuation through gelatin, unlike ferrofluids that spread uncontrollably under applied voltage. (**E**) Images of PTF's magnetic response in the sol state. Liganded MNPs prevent phase separation, enabling collective and dynamic motion under a magnetic field. (**F**) Rheological and electrical behavior of PTF. Reversible phase transition occurs while maintaining nearly constant conductivity. (**G**) Phase-transition cycling test. EG-based PTF maintains stable G', tan δ, and mass (wt %) over 20 cycles. Error bars show SD ($n = 3$). (**H**) Comparison of tan δ and viscosity among magnetoresponsive soft materials. Through phase transition, PTF achieves a unique combination of high elasticity and low viscosity.

mechanical actuation. A combination of a phase-transitional polymer network with a magnetoresponsive ferrofluid meets the foregoing material challenges. The resulting PTF exhibits soft and elastic properties in the gel state, enabling large areal actuation. In the sol state, it demonstrates dynamic behavior under a magnetic field, exhibiting easy movement and reconfiguration of the electrode.

The ability to reconfigure the electrode in DEA not only increases the flexibility in actuation but also enhances the sustainability of DEA (Fig. 1B). For instance, upon electrode disconnection, the electrode in the sol state self-heals to recover its original shape, thereby restoring actuation. Even in the case of dielectric breakdown, the damaged region can be cleared to retain actuation by reconstructing the circuit. Moreover, the electrode can be retrieved and reused after actuation, contributing to material recyclability and system longevity. These capabilities are especially valuable for DEAs that are inherently vulnerable to mechanical and electrical damage.

PTF is composed of liganded MNPs for magnetic response, EG as the solvent, gelatin as the phase-transitional matrix, and *N*-methylformamide (NMF) as the plasticizer (Fig. 1C and fig. S1). The ferrofluid, which exhibits a dynamic response under a magnetic field, maintains homogeneous colloidal stability through the surface ligands on the MNPs. Furthermore, these ligand-mediated interactions enable the MNPs and solvent to move collectively under a magnetic field, resulting in dynamic magnetic motion (*26*–*29*). To implement this strategy, liganded MNPs extracted from commercial aqueous ferrofluid [MICR (Magnetic Ink Character Recognition) ink] are used (fig. S2), enabling the stable and homogeneous colloidal state of the PTF. Gelatin was selected for its ability to undergo a reversible phase transition upon mild heating (around 30° to 40°C) (*30*, *31*). To retain the softness of the gelatin gel and enable prolonged usability, EG was used as the solvent with low volatility (*32*). NMF was added as a plasticizer to lower the viscosity of PTF, thereby increasing fluidic performance. For fabrication, gelatin was dissolved in the EG solvent with a plasticizer, and the MNPs were added, followed by homogeneous dispersion using a probe sonicator (fig. S3). The resulting PTF forms a soft and elastic gel through triple helices formed via hydrogen bonding between amide groups of gelatin chains. Upon heating to the sol state, the material demonstrates dynamic motion under an external magnetic field (fig. S4).

The resulting softness and stable gel state at room temperature allowed PTF to serve effectively as a DEA electrode, exhibiting stable actuation and large areal strain behavior (~169%) (Fig. 1D). In contrast, conventional ferrofluid that cannot undergo phase transition remains in the fluid state, making it difficult to retain its shape by spreading over a large area. In addition, PTF in the sol state exhibits homogeneous and collective motion without phase separation under a magnetic field, which was further confirmed by energy-dispersive x-ray spectroscopy (EDS) and scanning electron microscopy (SEM) analyses (Fig. 1E and movie S1). This behavior is mainly attributed to two factors. First, ligands on the MNP induce electrostatic repulsion and steric hindrance, preventing aggregation of nanoparticles (fig. S5). Second, in the EG environment, electrostatic attractions occur between positively charged gelatin and negatively charged liganded MNPs. Such interactions were further supported by Fourier transform infrared spectroscopy, in which the amide I band shifted from 1652 to 1635 cm^{-1} (fig. S6) (*33*). Thanks to these interactions, liganded MNPs, solvent, and polymer can move collectively under a magnetic field while maintaining colloidal stability. Therefore, when liganded MNPs are used, PTF exhibits good colloidal stability and collective motion under a magnetic field over an extended period (>120 min), unlike the PTF made of MNPs without ligands (fig. S7). Such characteristics enable dynamic reconfiguration of the PTF in response to various magnetic fields.

PTF offers reversible switching between solid-like and fluid-like properties via phase transition (Fig. 1F and movie S2). In addition, PTF features consistent ionic conductive behavior over a wide temperature range, showing its stable performance as an electrode (10° to 70°C) (figs. S8 and S9) (*34*). Furthermore, even after repeated phase-transition cycles, PTF exhibited excellent stability, showing no notable changes in storage modulus (G'), loss tangent (tan δ), mass, and conductivity (Fig. 1G and fig. S10). Owing to these characteristics, PTF can be demonstrated as an interconnect via electrically bridging nonconnected circuits in three-dimensional configurations (fig. S11). PTF can be lifted using a magnet to form electrical connections between disconnected circuits in the sol state. After gelation, even when the magnet is removed, the conductive bridge remains stable when stretched laterally because of the soft and stretchable nature of PTF. As a result, we developed a reconfigurable electrode that exhibits a low viscosity of 0.06 Pa·s and still achieves a low tan δ ($\delta = \frac{G''}{G'}$) of 0.03 in the gel state within a single system (Fig. 1H and table S1).

Mechanical and magnetodynamic properties of PTF

We screened various solvents to improve the softness and overall mechanical properties of the PTF as a DEA electrode. For this purpose, solvents should homogeneously mix with gelatin and exhibit a stable phase transition. Deionized (DI) water and EG were found to sustain a stable gel state at room temperature (figs. S12 and S13 and table S2). We compared various properties of PTFs prepared with DI water and EG as solvents. PTF(EG) showed a phase transition at ~48°C, whereas PTF(DI water) transitioned at around 34°C (Fig. 2A). This observation is consistent with previous reports that EG enhances hydrogen bonding within the gelatin's triple helix structure when used as a solvent (*35*, *36*). We then performed uniaxial tensile tests to assess the mechanical properties of the PTFs (Fig. 2B and fig. S14). Compared to PTF(DI water), PTF(EG) exhibited a modulus approximately two times lower, an elongation about 2.5 times higher, and a toughness roughly 3.3 times greater. This improvement is likely due to the limited ability of EG to form triple helix junctions in gelatin, resulting in shorter helices and longer coil regions, which make the material softer and more stretchable (*37*, *38*). Moreover, EG has a very low vapor pressure (0.011 kPa), which minimizes mass loss (<1%) in PTF(EG) at room temperature (Fig. 2C). In contrast, DI water has a higher vapor pressure (3.173 kPa), leading to rapid evaporation of PTF(DI water) under ambient conditions with a mass loss of ~62% for 5 hours. These mechanical properties can be tuned by adjusting the concentration of gelatin or MNPs (Fig. 2D and fig. S15).

To achieve the reconfigurability of the electrode, the material should have strong field responsiveness and low internal friction during motion. These properties are primarily governed by two factors: the fraction of MNPs and the viscosity of the PTF (Fig. 2E). Therefore, to achieve the dynamic magnetic responsiveness of PTF, it is necessary to increase the concentration of MNPs to increase magnetization (M) while simultaneously minimizing the internal resistance by lowering viscosity (η). For instance, when the MNP content is low, the magnetic force from an external field is insufficient

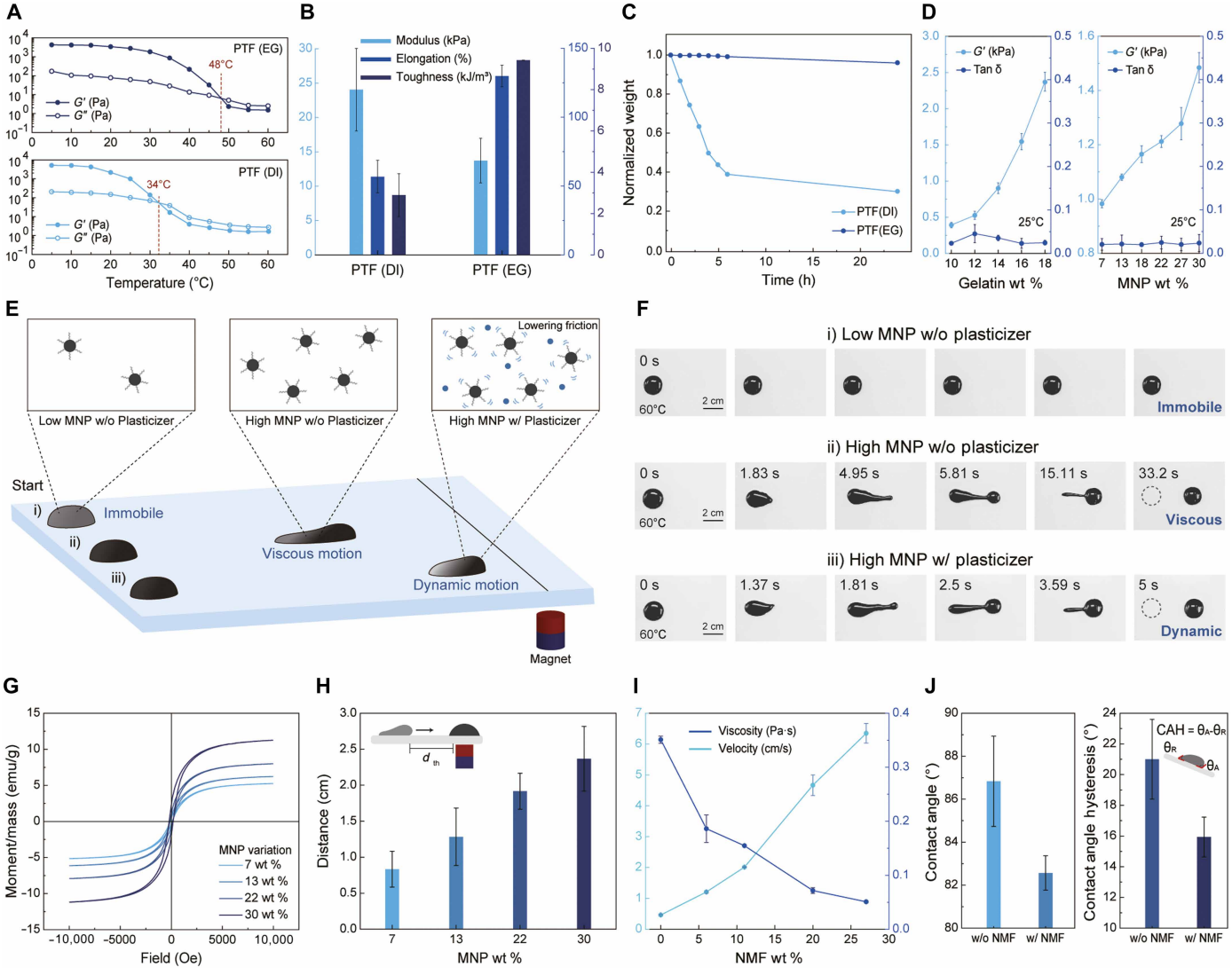

Fig. 2. Mechanical and magnetodynamic properties of PTF. (**A**) Rheological analysis of the phase-transition temperature of EG-based and DI-based PTFs. (**B**) Mechanical properties of PTFs in the gel state with EG and DI. A softer PTF with improved mechanical properties was obtained using EG. (**C**) Volatility test of PTF. EG-based PTF exhibits a lower vapor pressure than DI-based PTF. h, hours. (**D**) Rheological properties of PTF with various gelatin and MNP contents. (**E**) Magnetodynamic behavior is controlled by the concentrations of MNPs and plasticizer. (**F**) Snapshots of PTF with various MNP contents and plasticizer concentrations. A higher MNP content enhances magnetoresponsiveness, while a lower viscosity promotes dynamic motion. (**G**) Field-dependent magnetization curves of PTF at various MNP concentrations. (**H**) Threshold distance for magnetic response. The inset shows a schematic of the threshold distance (d_{th}), the critical point where initial PTF motion induces bulk material movement. (**I**) Viscosity of PTF with varying plasticizer fraction. The average velocity increases as the viscosity decreases. (**J**) CA and CAH with and without a plasticizer. The inset shows a schematic of CAH, defined as the difference between the advancing (θ_A) and receding (θ_R) angles. All measurements taken in the sol state were conducted at 60°C. Error bars show SD ($n = 3$).

to displace the PTF, provoking no observable movement [Fig. 2F (i)]. When both the MNP content and viscosity are high, PTF can move, but viscous resistance to motion leads to a slower response [Fig. 2F (ii)]. The optimal condition is realized when the MNP content is high and the viscosity is low [Fig. 2F (iii)]; under these conditions, the combination of strong magnetic force and low internal friction allows PTF to display highly dynamic motion under a magnetic field.

The field responsiveness of the PTF system was further analyzed by measuring its magnetization-magnetic field (*M-H*) curves (Fig. 2G). The absence of hysteresis in the *M-H* curves indicates that the material has superparamagnetic behavior (*39*). Its zero remanence and rapid magnetic response make it ideal for reversible magnetic reconfiguration. In addition, the saturation magnetization (M_s) of PTF also increased as the MNP fraction increased, indicating that more nanoparticles could align with the external magnetic field. Correspondingly, PTFs with a higher MNP content responded to magnets positioned at longer distances (Fig. 2H).

The viscosity of PTF also plays a crucial role in its dynamic reconfiguration. EG alone has a high viscosity (15.6 mPa·s) (*40*), which substantially hinders the PTF mobility. To address this, NMF was added as a plasticizer to reduce the viscosity. NMF has a low

viscosity (1.6 mPa·s) (*41*), a low vapor pressure (0.06 kPa) (*42*), and a high boiling point (199.5°C) (*43*) and shows homogeneous miscibility with gelatin, making it an ideal plasticizer for PTF. Specifically, we measured the velocity of PTF in the sol state, defined as the average velocity at which the entire PTF is pulled toward a magnet, with varying NMF concentrations. PTF containing 27.5 wt % NMF exhibited a 13.6-fold increase in speed compared to PTF without NMF (Fig. 2I and fig. S16). However, excessive NMF content disrupts the formation of the gelatin's triple helix structure, lowering the phase-transition temperature and compromising the performance of the gel state (fig. S17). Therefore, 20 wt % NMF was selected as the optimal concentration to balance the sol dynamicity and gel stability. To support the enhancement of PTF's dynamic behavior upon NMF addition, we measured the contact angle (CA) and contact angle hysteresis (CAH) of PTF drops in the sol state on Ecoflex (Fig. 2J and fig. S18). In the presence of NMF, PTF exhibited a lower CA, indicating improved surface conformability. Furthermore, a lower CAH implies that PTF can move more readily across the surface, supporting its high reconfigurability.

rDEAs with PTF

We aimed to explore the potential of PTF as an electrode for DEAs (Fig. 3A). Under DEA operation, given that the voltage applied by the PTF is very low (*8*), no electrochemical reactions occur, and the PTF operates safely as the electrode (fig. S19). Compared to carbon grease, which is widely used as an electrode for DEAs because of its moderate electrical conductivity and low elastic modulus (*44*), PTF exhibited negligible strain differences across commonly used dielectric materials [PDMS (polydimethylsiloxane), Ecoflex, and VHB] in DEAs (Fig. 3B). Moreover, because of the compliant and soft nature of PTF, the DEA with VHB yielded a large areal strain of 169% under an electric field of 81 MV/m. To evaluate the resilience of the PTF electrode, we analyzed its areal strain after repeated phase transitions on the dielectric surface (Fig. 3C). After six cycles of phase transition, PTF still maintained stable strain behavior without noticeable degradation. Moreover, DEA using a PTF electrode exhibited consistent actuation over 4000 cycles without performance loss, demonstrating its robustness as an electrode material (Fig. 3D and fig. S20).

The ability to perform phase transition directly on the dielectric surface critically helps PTF to form reliable, conformal contact with the substrate. The seamless interfacial adhesion between the electrode and dielectric was confirmed by SEM imaging (Fig. 3E and fig. S21). When PTF was transferred onto the dielectric after being prepared elsewhere, the insufficient contact resulted in poor adhesion. As a result, slip occurred once the applied electric field exceeded a certain level. Consequently, only 9.6% areal strain was achieved at 36 MV/m (Fig. 3F and fig. S22). In contrast, direct phase transition on the dielectric resulted in robust actuation without slip, delivering an areal strain of 41% at 36 MV/m—4.2 times higher than the transferred case (movie S3).

The merits of direct phase transition become even more pronounced when the dielectric layer is contaminated. In such a case, the contact area between the electrode and the dielectric is markedly reduced, making actuation more challenging. However, when the electrode is formed via phase transition, the fluidic nature of PTF allows it to efficiently infiltrate uncontaminated regions, bypassing contaminants and achieving a highly conformal interface with the contaminated dielectric (Fig. 3G). While transferred PTF failed to establish intimate contact with the dielectric, resulting in negligible actuation—only 5.9% areal strain at 36 MV/m (Fig. 3H and fig. S23)—phase-transitioned PTF yielded improved performance, achieving a much higher areal strain of 21% under the same field condition.

By exploiting the resilient yet dynamic properties of PTF, we developed a platform for rDEA, previously unachievable with conventional systems (Fig. 3I). Conventional DEAs, once designed, can only operate within a predefined geometry. In contrast, after PTF performs actuation at an initial position, transitioning to the sol state renders the electrode reconfigurable, allowing it to move to a new location and adopt a different geometry. Furthermore, the excellent fluidity in the sol state enables it to be split into two independent components, which can then be individually reconfigured to produce distinct actuation patterns (movie S4). To visualize the reconfiguration and actuation of the PTF, we used a transparent organogel electrode on the bottom side. This rDEA is not only limited to simple planar configurations but is also applicable to bending actuators (Fig. 3J and fig. S24). By adjusting the overlapping area between the PTF electrode and the dielectric layer of the bending actuator, the degree of bending can be controlled. Specifically, as the contact area between the dielectric and the PTF increases, both the bending angle (20° → 30° → 41.7°) and bending force (14.1 mN → 22.4 mN → 32.6 mN) tend to increase linearly (Fig. 3K, fig. S25, and movie S5). This control strategy offers an advantage over voltage-based actuation control, as it enables multiple actuation configurations to be generated from a single voltage source (fig. S26).

The application of a reconfigurable PTF electrode is not limited to DEAs alone but can also be extended to other areas, such as stretchable devices and electroluminescent displays (figs. S27 and S28). In the sol state, the electrode can freely move within the luminescent layers, allowing the realization of highly reconfigurable in situ displays. In the gel state, optical information can be stored in specific locations. Notably, the stored information remains stable even under external magnetic fields, enabling reversible writing and erasing of optical information over repeated cycles. This functionality opens up possibilities for building electronic systems with increased complexity and functional adaptability (fig. S29 and movie S6). For instance, PTF can navigate through narrow gaps and rejoin after passing through obstacles. Beyond simple two-dimensional configurations, PTF can also be split vertically into the three-dimensional space, enabling individual units to perform distinct functions. Therefore, we were able to simultaneously operate electroluminescent displays and DEA actuation using spatially separated PTFs. Furthermore, the DEA and alternating current (ac) electroluminescence display can be combined, enabling the actuator to incorporate display functionality (fig. S30). Through reconfiguration, the combined device can generate new visual patterns while performing mechanical actuation.

Increased sustainability of DEA by PTF

The rDEA enabled by PTF not only allows for in situ manipulation of actuation but also offers practical benefits for increasing the sustainability of DEAs. When the PTF electrode in a DEA is damaged, phase transition can be used to restore the disconnected electrode (Fig. 4A). Beyond such recovery of damaged electrodes, PTF-based DEAs can also address other failure modes. In cases where a malfunction arises from electrical breakdown or mechanical puncture, magnetic reconfiguration can isolate the shorted pathway, allowing the system to recover normal actuation behavior (Fig. 4B). Moreover,

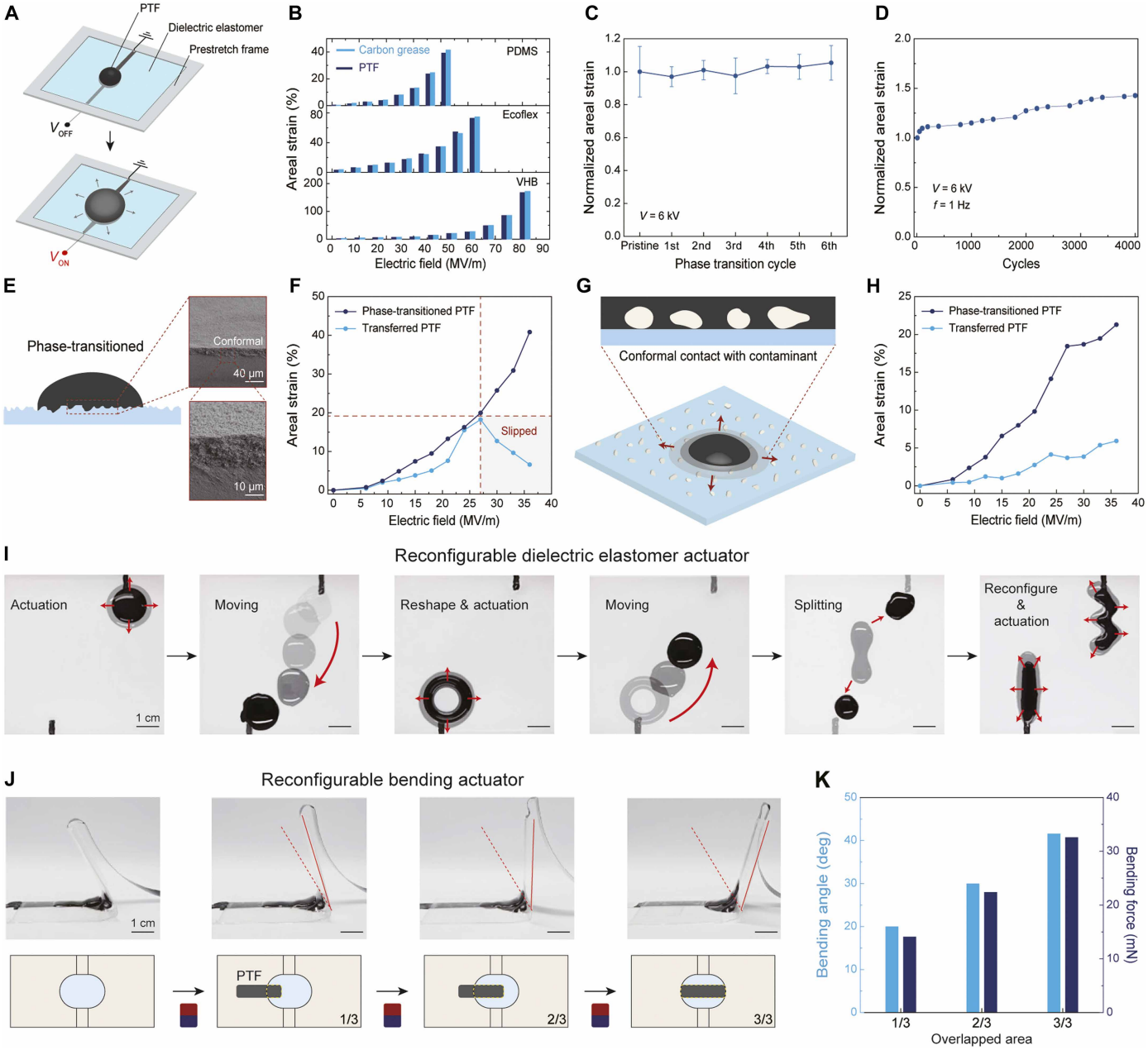

Fig. 3. rDEAs with PTF. (**A**) Schematic illustration of DEA actuation with a PTF electrode. (**B**) Areal strain in PTF-based DEAs using various dielectric materials. Strain is identical to conventional carbon grease electrodes. (**C**) Areal strain over phase transition cycles. PTF-based DEA shows consistent maximum strain through six transition cycles. (**D**) Cyclic actuation performance over 4000 cycles. (**E**) Schematics and SEM images of the conformal interface between PTF and a dielectric. (**F**) Comparison of areal strain between transferred and phase-transitioned PTFs. Transferred PTF slips resulting from poor contact with the dielectric surface. (**G**) Schematics of the conformal contact on a contaminated surface with phase-transitioned PTF. (**H**) Maximum areal strain of contaminated DEAs. Phase-transitioned PTF enables actuation even in contaminated environments because of its excellent conformability. (**I**) Highly reconfigurable DEA using PTF. (**J** and **K**) Bending actuator with PTF. Electrode reconfiguration allows tuning of bending angle and output force by adjusting the fraction of the PTF electrode area overlapped with the bottom carbon grease electrode area. Error bars show SD ($n = 3$).

thanks to the phase-transitional nature of PTF, it can be retrieved from the DEA in its sol state, stored, and later reused, demonstrating its sustainability (Fig. 4C).

We examined these sustainable features in more detail. Figure 4D demonstrates a self-healing PTF electrode. To emulate an electrode disconnection caused by external conditions, we manually cut the PTF. In the sol state, the fluidic nature of PTF allows the damaged electrode to reconnect under an applied magnetic field. Once rejoined, the PTF forms a unified gel and recovers its original actuation performance through phase transition (movie S7). We also address one of the most common failure modes in DEA operation, dielectric breakdown. When excessive voltage is applied beyond the dielectric strength, electrical trees can propagate through the dielectric layer, eventually leading to a short circuit (*45*, *46*). In conventional

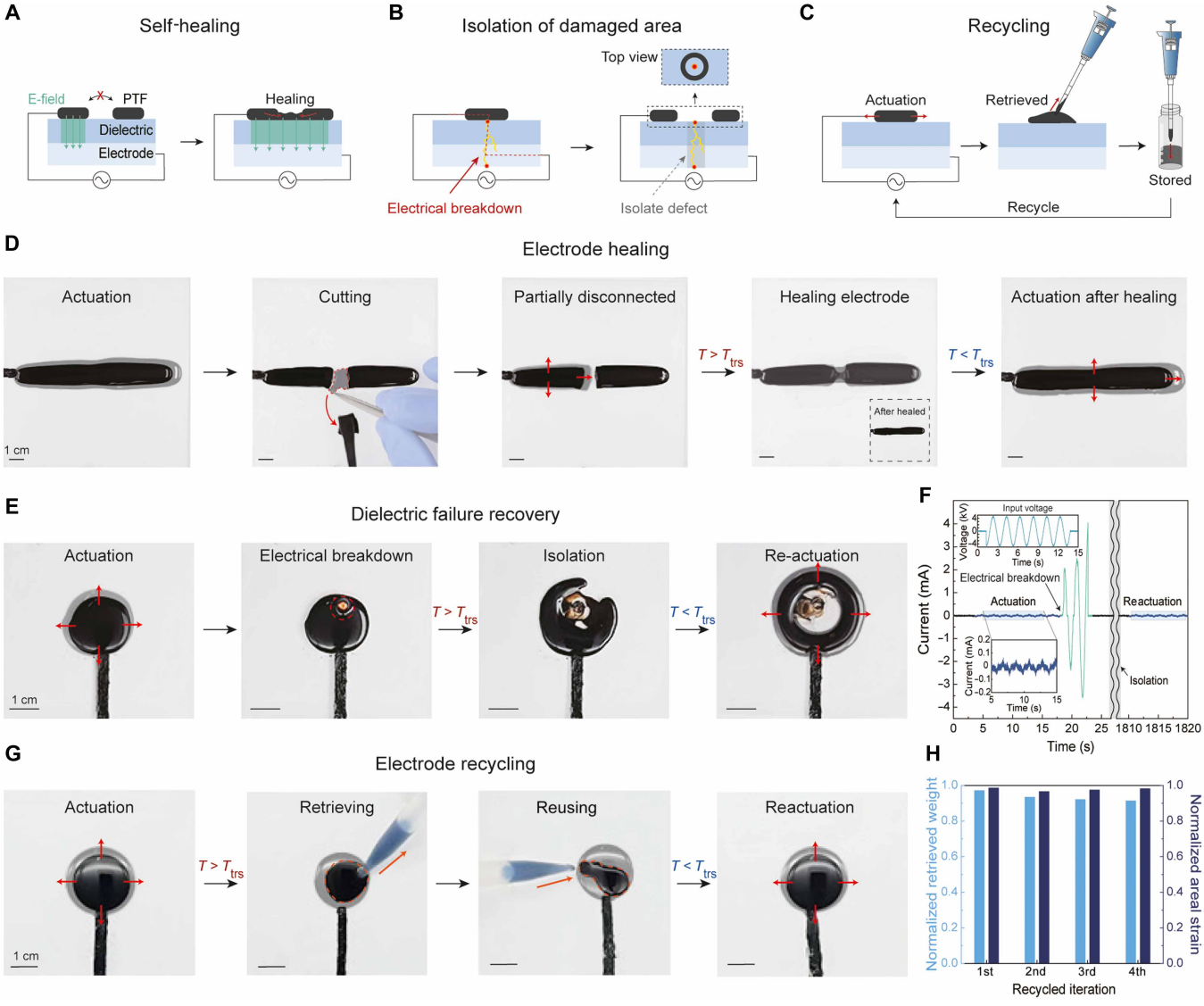

Fig. 4. Increased sustainability of DEAs by PTF. (**A**) Schematic illustration of self-healable PTF. A disconnected electrode in a DEA can be reconnected via phase transition, enabling restoration of actuation. (**B**) Schematic illustration of DEA breakdown and its recoverability using PTF. Magnetic reconfiguration isolates the damaged region and thus resumes actuation. (**C**) Schematic illustration of PTF reutilization. Through phase transition to the sol state, PTF can be retrieved, stored, and then reused on-demand. (**D**) Self-healing procedure of PTF on DEA. By inducing a phase transition to the sol state, disconnected circuits can be restored, allowing the recovery of their original operation. T_{trs} represents the PTF's transition temperature (42.5°C). (**E**) Isolation of damaged area through PTF reconfiguration. (**F**) Electrical signals measured during the DEA breakdown recovery process. The inset shows the signal profile of the applied voltage. (**G**) Reuse of the PTF electrode in DEA. PTF can be retrieved and reused. (**H**) Areal strain and retrieved weight of PTF over multiple cycles.

DEAs, such breakdowns often render the device unusable, severely limiting its operational lifespan. However, PTF offers a way to overcome this limitation. Through magnetic reconfiguration, PTF selectively excludes the failed region from the active circuit (Fig. 4E and movie S8). As a result, the actuator continues to operate stably when the original signal is reapplied, even in an electrically failed system (Fig. 4F). This strategy is effective against not only electrical failure but also mechanical damage such as punctures from piercing or scratching (fig. S31). Punctures by metallic objects, for example, can bring the bottom electrode into direct contact with the top electrode (*47*). In such cases, magnetic reconfiguration can be used to isolate the punctured region, enabling the system to resume reliable actuation (movie S9). Through this dynamic reconfiguration strategy, the system exhibits robust sustainability even under harsh conditions involving electrical failure or physical damage. While several practical methods for electrode repair (*48*–*50*) and self-clearing (*51*–*54*) exist, our approach uniquely enables both the functions on demand using a noncontact magnetic field, providing clear operational advantages. Furthermore, repeated actuation cycles can lead to performance degradation and mechanical fatigue in DEAs, ultimately rendering the device unusable. In such cases, entire devices are often discarded, even when most components remain functional. By using the

PTF electrode in DEA, it can be easily extracted in its sol state, stored stably over time, and reapplied to a new or repaired device when needed (Fig. 4G). Notably, PTF demonstrates a high recovery yield (~91%) even after multiple retrieval cycles (Fig. 4H). When reused, it consistently delivers areal strain comparable to its initial performance, ensuring reproducible actuation. Therefore, the ability to achieve failure recovery through self-healing and electrode clearing, along with the eco-friendly reusability of materials, represents a creative and promising approach to overcoming the limitations of conventional DEAs.

DISCUSSION

In this study, we introduce a reconfigurable electrode for DEAs by integrating a sol-gel–transitional polymer with liganded MNPs from ferrofluid. In the sol state, optimized nanoparticle-polymer-solvent interactions and plasticizer-induced viscosity reduction render the system magnetodynamic and highly reconfigurable. In the gel state, the EG-based gelatin matrix maintains softness and stability, enabling large areal actuation without compromising DEA performance during repeated phase transitions. By combining solid-like and fluid-like properties, the electrode permits on-demand actuation in diverse shapes and locations within a single device. Its conformability ensures strong adhesion even on contaminated surfaces, while reconfigurability restores actuation after electrode or dielectric failure and allows retrieval with a high recycling efficiency (~90%). The PTF reframes electrodes from static conductors to reprogrammable elements, establishing DEAs as field-programmable platforms with enhanced versatility and durability. The demonstrated reconfigurability illustrates how a single actuator can generate diverse actuation, thereby advancing toward the bioinspired goal of emulating human muscles with intrinsic high degrees of freedom. Consequently, by overcoming the long-standing trade-off between performance and flexibility in traditional DEAs, the PTF establishes a broadly applicable foundation for multifunctional soft robotics, artificial muscles, and next-generation soft electronic systems requiring intrinsic adaptability. While the present demonstrations focus on planar and simple bending DEAs, further optimization of the materials could enable integration into more advanced architectures, including multilayered stacks and pixel-patterned arrays, which are active areas of ongoing research.

MATERIALS AND METHODS

Materials

Gelatin (gel strength ~175 g, Bloom, Type A), NMF (99%), lithium phenyl-2,4,6-trimethylbenzoylphosphinate (LAP), *N*,*N*′-methylenebis(acrylamide) (MBAA), and 4-hydroxybutyl acrylate (HBA) were purchased from Sigma-Aldrich. EG (99%) was obtained from Duksan. Cobalt ferrite ($CoFe_2O_4$) nanoparticles (99.9%, ~30 nm) were purchased from Korea Nanomaterials. ZnS:Cu phosphor particles were obtained from Lonco Company Limited (LP-6861). NdFeB magnets were obtained from JL Magnet. VHB 4910 (3M), Ecoflex 00-20 (Smooth-On), and Sylgard 186 (Dow Corning) were used as dielectric layers. Carbon grease (MG Chemicals, Carbon Conductive Grease, 846-80G) was used as the control electrode. VersaInk MICR was used as an aqueous ferrofluid. Unless otherwise noted, all MNPs refer to liganded MNPs extracted from MICR. Ultrapure water was prepared using a Milli-Q purification system.

Synthesis of PTF

To obtain MNPs, VersaInk MICR was mixed with DI water at a volume ratio of 2:1 and centrifuged at 10,000 rpm for 5 hours. The supernatant was discarded, and the precipitate was redispersed in 30 ml of DI water followed by an additional centrifugation under the same conditions. After discarding the supernatant again, the remaining precipitate was collected and vacuum dried at 60°C overnight. Gelatin at 16 wt % relative to EG was added and stirred at 60°C for 1 hour. Subsequently, MNPs and an NMF plasticizer at 30 and 20 wt %, respectively, were added to the mixture, followed by mechanical stirring for 30 min. The mixture was then homogenized using sonication for an additional 30 min.

Volatility test

For volatility measurements under ambient conditions, the PTF samples were left in air at room temperature. Their weight was measured every hour. For volatility measurements after repeated phase transitions, the PTF samples were heated at 60°C for 10 min and then cooled at 4°C for 2 hours. Afterward, the samples were left at room temperature for 30 min, and their weight was measured again.

Colloidal stability test

The PTF sample was placed in a cuvette, and to prevent gelation during measurement, the temperature was maintained using a hot plate placed underneath. Real-time transmittance was then measured using a spectrometer (FLAME-S, Ocean Optics). In addition, the homogeneity of PTF was examined using scanning electron microscopy (field-emission SEM–EDS, AURIGA). The zeta potential was measured using a DLS instrument (ELS Z-neo). For these measurements, the concentrations of particles and gelatin were adjusted to 0.2 and 0.15 mg/ml, respectively, before analysis.

Rheological property measurement

The viscoelastic properties of PTF were analyzed using a rheometer (DHR-2, TA Instruments). PTF samples were prepared in a disc shape with a diameter of 20 mm and a thickness of 2 mm. For the frequency sweep test, the angular frequency was set from 0.1 to 100 rad/s with a constant strain of 2%. The rheological loss factor, tan δ, was defined as the ratio of the loss modulus (G'') to the storage modulus (G') at 1 Hz. For the temperature sweep test, a disc-shaped acrylic mold was first fixed onto the parallel plate geometry of the rheometer. The sol-state sample was poured into the acrylic mold and was left at 5°C for 2 hours. The temperature was then increased at a rate of 5°C/min. For samples with NMF as the solvent, the temperature sweep rate was set to 2°C/min.

For viscosity measurements, the disc-shaped acrylic mold (a diameter of 20 mm and a thickness of 2 mm) was mounted on the rheometer's parallel plate, and the sol-state sample was poured into the mold. After holding at 60°C for 10 min, the viscosity at 60°C was recorded under a 2% strain over a shear rate sweep from 0.01 to 100 s^{-1}.

Dynamic responsiveness measurements

The dynamic sol-state responsiveness of PTF was evaluated on a Teflon-coated acrylic plate. Equal volumes of PTF sol were dropped at the same starting position, and the threshold distance was measured by adjusting the position of a magnet. For CA and CAH measurements, a CA analyzer (FEMTOFAB, Smart Drop) was used. A 5-μl droplet of each sample was deposited onto the Ecoflex. CAH was determined by tilting the stage at a rate of 3°/s.

Characterization of mechanical properties

Samples for the mechanical test were prepared in a rectangular shape with dimensions of 10 mm by 30 mm. Acrylic sheets were used as the gripping surface for the mechanical test. The samples were fixed to the grippers using Krazy glue and loaded onto a universal testing machine (Instron 3343) equipped with a 50-N load cell. The gauge length was set to 5 mm. The tensile speed was set to 5 mm/min.

TGA (thermogravimetric analysis) was performed on both liganded MNPs and ligand-free $CoFe_2O_4$ particles by heating from 30° to 800°C at 10°C/min using a Discovery TGA 5500. Transmission electron microscopy samples were prepared by dispersing liganded MNPs in ethanol (~0.1 wt %), dropping 2 μl onto a grid, and drying at 40°C for 48 hours. Morphology was examined with a JEM-2100F. X-ray diffraction peak analysis of both particle types was carried out on a D8 Advance diffractometer.

The ionic conductivity of PTF samples was determined by analyzing impedance spectra obtained from an LCR meter (Agilent, E4980A). The instrument was equipped with a dielectric test fixture and analysis software (16451B and N1500A) and operated over a frequency range of 20 Hz to 1 MHz.

Temperature dependent conductivity was measured using a Concept-40 BDS (broadband dielectric spectroscopy) system (Novo Control) equipped with DETACHEM software. Measurements were performed using BDS 1301 gold-plate electrodes. The sample, initially in liquid form, was injected into a CR2032-type coin cell mold with a thickness of 2.8 mm and solidified at room temperature before measurement. Conductivity was measured from 10° to 70°C in 10°C intervals. At each temperature point, the sample was held for 10 min to ensure thermal equilibration before measurement. During the characterization process, an ac signal of 1 V_{rms} was applied, and the temperature was increased at a rate of 10°C/min.

The magnetic properties of PTF were measured using a vibrating sample magnetometer (VSM-7410, Lakeshore). The sample was prepared using the KBr pellet method and analyzed with a Fourier transform infrared spectrometer (Nicolet iS50) over a wavenumber range of 4000 to 400 cm^{-1}.

Fabrication and characterization of DEA using various dielectric materials

VHB 4910 (1 mm thick), Ecoflex 00-20 (750 μm thick), and polydimethylsiloxane (Sylgard 186, 400 μm thick) films were prestretched by factors of 3 by 3, 2.5 by 2.5, and 1.75 by 1.75, respectively, and then bonded to a 3-mm-thick poly(methyl methacrylate) rigid frame (inner dimensions: 100 mm by 100 mm; outer dimensions: 130 mm by 130 mm). One side of each prestretched frame was treated with O_2 plasma for 2 min (Femto Science, COVANCE), after which 5 ml of soft organogel solution was poured onto the surface. The organogel solution was prepared by mixing 15 ml of HBA, 70 ml of EG, 0.02 g of MBAA, and 1 ml of a 3 wt % LAP solution in DI water for 6 hours. Polymerization was carried out under 365-nm ultraviolet irradiation (CL-1000L, UVP) for 5 min to form a transparent electrode. Unless otherwise noted, all dielectric materials of DEA devices refer to Ecoflex-coated VHB. For electrical actuation, carbon grease was used to connect the PTF layer to an external electrode made from carbon tape. A waveform was programmed on a function generator (Agilent 33612A) and amplified 3000-fold by a high-voltage amplifier before being applied to the DEA. Unless otherwise mentioned, all actuation behaviors were recorded using a digital single-lens reflex camera. Areal strain (ε_a) was calculated from the recorded images using ImageJ software according to $\varepsilon_a = \frac{a_1 - a_0}{a_0} \times 100\,\%$, where a_1 is the actuated area under high voltage, and a_0 is the initial area.

Cyclic test of DEA

For conventional cyclic testing, the DEA was cycled at 50 MV/m and 2 Hz. The normalized strain a_n was defined as $a_n = \frac{a_1}{a_0}$, where a_0 is the initial areal strain, and a_1 is the actuated areal strain after phase transition or cyclic testing. For phase-transition cyclic test, the DEA was actuated at 50 MV/m and 500 mHz for 2 min. The sample was then melted and allowed to solidify at room temperature for 30 min. Last, it was actuated under the previously described condition.

Fabrication and operation of the reconfigurable bending actuator

First, polyethylene terephthalate (PET) films for the 0.1-mm-thick substrate layer and the 0.25-mm-thick reinforcement layer were laser cut into the desired shapes. Next, VHB 4910 was prestretched by 3.5 by 3.5 and clamped in an acrylic frame. A PET support frame was then bonded on top of the stretched VHB. The assembly was mounted reinforcement-side up on a spin coater (ACE-20) and coated with 1.5 ml of Ecoflex 00-20 at 400 rpm for 120 s. This Ecoflex coating is intended to facilitate the reconfiguration of the PTF, and it is so thin that its effect on the DEA performance is negligible (fig. S32). After coating, the structure was cured at 60°C for 3 hours. Once cured, the soft actuator was released from its fixation frame and trimmed to its final form. For bending actuation, carbon grease served as the counter electrode on the substrate-PET side, while PTF was applied to the reinforcement-PET side and the actuator was driven to bend. The effective overlap area between the dielectric and PTF was adjusted by horizontally attaching three 5 mm–by–5 mm NdFeB magnets, and actuation was driven by a 100-mHz, 6-kV electrical signal. The bending force was measured by attaching a force-gauge tip (MARK-10, Series 7) to the bending actuator.

Fabrication and operation of reconfigurable luminescent display

The reconfigurable luminescent display consists of two indium tin oxide (ITO)-glass panels (120 mm by 120 mm). For the luminescent layer, a composite of Ecoflex 00-20, ZnS:Cu^+, and $BaTiO_3$ (10:1:1 wt %) was prepared by mixing in a Thinky mixer (ARE-310) at 2000 rpm for 2 min, followed by degassing at 2200 rpm for 2 min. Five milliliters of this mixture was then spin-coated onto one ITO glass at 400 rpm for 120 s and cured at 60°C for 3 hours.

For the lubricant layer, the second ITO glass was coated with Teflon tape (ALPHAFLON, 80 μm thick). This Teflon coating was applied to facilitate the reconfiguration of the PTF. The two ITO-glass panels were then spaced 2 mm apart using acrylic strips (2 mm by 100 mm). A 500-μl drop of PTF was introduced between the panels, and an electrical signal (2 kHz, 1.5 kV) was applied. The voltage across the PTF and the top ITO glass produced luminescence, and moving the PTF in this state enabled an in situ luminescent display.

To store the displayed pattern, the PTF was left under ambient conditions for 30 min to solidify, after which the electrical signal was reapplied. To erase and reconfigure the PTF, the solidified PTF was remelted using a custom-built heat gun.

Fabrication and operation of DEA with ac electroluminescence

Reconfigurable luminescent display with DEA devices was fabricated using a composite mixture of Ecoflex 00-20, ZnS:Cu^+, and $BaTiO_3$ powders (10:1:1 wt %). The constituents were combined in a Thinky mixer (ARE-310) at 2000 rpm for 2 min and subsequently degassed at 2200 rpm for 2 min. The resulting elastomer composite was prestretched by a factor of 2.5 by 2.5 and fixed onto a 3-mm-thick poly(methyl methacrylate) rigid frame to form the device. Electrical excitation of the ac electroluminescent layer was achieved by applying a 1.5-kV, 2-kHz ac signal, and mechanical actuation was induced by introducing an offset to the driving waveform.

DEA recovery by magnetic reconfiguration

In this experiment, a VHB-based DEA structure, as previously described, was used. The counter electrode consisted of organogel coated with a thin layer of Ecoflex, following the same procedure outlined earlier. Subsequently, 600 μl of PTF was applied, and initial DEA actuation was performed using an electric signal of 4.5 kV at 500 mHz. A brief high-voltage pulse of 15 kV was then applied to induce dielectric breakdown of the DEA. When 4.5 kV was reapplied afterward, no actuation was observed, confirming the failure. To create an open circuit at the damaged region, PTF underwent phase transition, and a ring-shaped pattern was formed, excluding the affected area. After allowing gelation to proceed at room temperature for 30 min, an electric signal of 4.5 kV was reapplied, successfully triggering reactuation.

Supplementary Materials

The PDF file includes:

Figs. S1 to S32
Tables S1 and S2
Legends for movies S1 to S9
References

Other Supplementary Material for this manuscript includes the following:

Movies S1 to S9

REFERENCES

1. Y. Lee, W. J. Song, J.-Y. Sun, Hydrogel soft robotics. *Mater. Today Phys.* **15**, 100258 (2020).
2. Y. Lee, W. J. Song, Y. Jung, H. Yoo, M.-Y. Kim, H.-Y. Kim, J.-Y. Sun, Ionic spiderwebs. *Sci. Robot.* **5**, eaaz5405 (2020).
3. J. Shintake, V. Cacucciolo, D. Floreano, H. Shea, Soft robotic grippers. *Adv. Mater.* **30**, 1707035 (2018).
4. W. J. Song, Y.-W. Kang, Y. H. Lee, J. Kim, B. F. G. Aymon, S.-Y. Choi, Y. E. Cho, X.-Y. Yan, S. Li, Y. Lee, X. Zhao, Y.-L. Park, J.-Y. Sun, All-3D-printed multi-environment modular microrobots powered by large-displacement dielectric elastomer microactuators. *Adv. Mater.* **37**, e07503 (2025).
5. C. S. Park, Y.-W. Kang, H. Na, J.-Y. Sun, Hydrogels for bioinspired soft robots. *Prog. Polym. Sci.* **150**, 101791 (2024).
6. V. Cacucciolo, J. Shintake, Y. Kuwajima, S. Maeda, D. Floreano, H. Shea, Stretchable pumps for soft machines. *Nature* **572**, 516–519 (2019).
7. T. J. Wallin, J. Pikul, R. F. Shepherd, 3D printing of soft robotic systems. *Nat. Rev. Mater.* **3**, 84–100 (2018).
8. C. Keplinger, J.-Y. Sun, C. C. Foo, P. Rothemund, G. M. Whitesides, Z. Suo, Stretchable, transparent, ionic conductors. *Science* **341**, 984–987 (2013).
9. D. Y. Kim, S. Choi, H. Cho, J.-Y. Sun, Electroactive soft photonic devices for the synesthetic perception of color and sound. *Adv. Mater.* **31**, e1804080 (2019).
10. E. Acome, S. K. Mitchell, T. Morrissey, M. Emmett, C. Benjamin, M. King, M. Radakovitz, C. Keplinger, Hydraulically amplified self-healing electrostatic actuators with muscle-like performance. *Science* **359**, 61–65 (2018).
11. X. Ji, X. Liu, V. Cacucciolo, M. Imboden, Y. Civet, A. El Haitami, S. Cantin, Y. Perriard, H. Shea, An autonomous untethered fast soft robotic insect driven by low-voltage dielectric elastomer actuators. *Sci. Robot.* **4**, eaaz6451 (2019).
12. Z. Suo, Theory of dielectric elastomers. *Acta Mech. Solida Sin.* **23**, 549–578 (2010).
13. X. Zhao, Z. Suo, Theory of dielectric elastomers capable of giant deformation of actuation. *Phys. Rev. Lett.* **104**, 178302 (2010).
14. G. Gu, J. Zou, R. Zhao, X. Zhao, X. Zhu, Soft wall-climbing robots. *Sci. Robot.* **3**, eaat2874 (2018).
15. Y. Chen, H. Zhao, J. Mao, P. Chirarattananon, E. F. Helbling, N.-S. P. Hyun, D. R. Clarke, R. J. Wood, Controlled flight of a microrobot powered by soft artificial muscles. *Nature* **575**, 324–329 (2019).
16. G. Sung, C. Yu, J.-M. Park, Y. H. Lee, C. S. Park, H. Lee, M. S. Kwon, J.-Y. Sun, High-k zwitterionic dielectric elastomers with internal plasticization for low-voltage actuation. *Mater. Today* **88**, 109–116 (2025).
17. J.-M. Park, C. S. Park, S. K. Kwak, J.-Y. Sun, Glass transition temperature as a unified parameter to design self-healable elastomers. *Sci. Adv.* **10**, eadp0729 (2024).
18. E. Hajiesmaili, D. R. Clarke, Dielectric elastomer actuators. *J. Appl. Phys.* **129**, 151102 (2021).
19. E. Hajiesmaili, N. M. Larson, J. A. Lewis, D. R. Clarke, Programmed shape-morphing into complex target shapes using architected dielectric elastomer actuators. *Sci. Adv.* **8**, eabn9198 (2022).
20. E. Hajiesmaili, D. R. Clarke, Reconfigurable shape-morphing dielectric elastomers using spatially varying electric fields. *Nat. Commun.* **10**, 183 (2019).
21. J. Wang, S. Li, D. Gao, J. Xiong, P. S. Lee, Reconfigurable and programmable origami dielectric elastomer actuators with 3D shape morphing and emissive architectures. *NPG Asia Mater.* **11**, 71 (2019).
22. H. Fu, Y. Jiang, J. Lv, Y. Huang, Z. Gai, Y. Liu, P. S. Lee, H. Xu, D. Wu, Multilayer dielectric elastomer with reconfigurable electrodes for artificial muscle. *Adv. Sci.* **10**, 2206094 (2023).
23. B. Aksoy, H. Shea, Reconfigurable and latchable shape-morphing dielectric elastomers based on local stiffness modulation. *Adv. Funct. Mater.* **30**, 2001597 (2020).
24. A. Chortos, J. Mao, J. Mueller, E. Hajiesmaili, J. A. Lewis, D. R. Clarke, Printing reconfigurable bundles of dielectric elastomer fibers. *Adv. Funct. Mater.* **31**, 2010643 (2021).
25. S. Rosset, H. R. Shea, Flexible and stretchable electrodes for dielectric elastomer actuators. *Appl. Phys. A* **110**, 281–307 (2013).
26. X. Fan, X. Dong, A. C. Karacakol, H. Xie, M. Sitti, Reconfigurable multifunctional ferrofluid droplet robots. *Proc. Natl. Acad. Sci. U.S.A.* **117**, 27916–27926 (2020).
27. X. Fan, Y. Jiang, M. Li, Y. Zhang, C. Tian, L. Mao, H. Xie, L. Sun, Z. Yang, M. Sitti, Scale-reconfigurable miniature ferrofluidic robots for negotiating sharply variable spaces. *Sci. Adv.* **8**, eabq1677 (2022).
28. W. Wang, J. V. Timonen, A. Carlson, D.-M. Drotlef, C. T. Zhang, S. Kolle, A. Grinthal, T.-S. Wong, B. Hatton, S. H. Kang, S. Kennedy, J. Chi, R. T. Blough, M. Sitti, L. Mahadevan, J. Aizenberg, Multifunctional ferrofluid-infused surfaces with reconfigurable multiscale topography. *Nature* **559**, 77–82 (2018).
29. M. Sun, S. Yang, J. Jiang, S. Jiang, M. Sitti, L. Zhang, Bioinspired self-assembled colloidal collectives drifting in three dimensions underwater. *Sci. Adv.* **9**, eadj4201 (2023).
30. M. Baumgartner, F. Hartmann, M. Drack, D. Preninger, D. Wirthl, R. Gerstmayr, L. Lehner, G. Mao, R. Pruckner, S. Demchyshyn, L. Reiter, M. Strobel, T. Stockinger, D. Schiller, S. Kimeswenger, F. Greibich, G. Buchberger, E. Bradt, S. Hild, S. Bauer, M. Kaltenbrunner, Resilient yet entirely degradable gelatin-based biogels for soft robots and electronics. *Nat. Mater.* **19**, 1102–1109 (2020).
31. T. Li, H. Qi, C. Zhao, Z. Li, W. Zhou, G. Li, H. Zhuo, W. Zhai, Robust skin-integrated conductive biogel for high-fidelity detection under mechanical stress. *Nat. Commun.* **16**, 88 (2025).
32. Y. H. Lee, W. J. Song, J.-M. Park, G. Sung, M.-G. Lee, M. Kim, S. Park, J. S. Lee, M. Kim, W. S. Kim, J.-Y. Sun, Full-color generation via phototunable mono ink for fast and elaborate printings. *Adv. Mater.* **35**, e2307165 (2023).
33. F. Gao, H. Jiang, D. Wang, S. Wang, W. Song, Bio-inspired magnetic-responsive supramolecular-covalent semi-convertible hydrogel. *Adv. Mater.* **36**, 2401645 (2024).
34. H. Yoo, Y. H. Lee, M.-G. Lee, J.-Y. Sun, Gel-based ionic circuits. *Chem. Rev.* **125**, 8956–9011 (2025).
35. I. S. Chronakis, S. Kasapis, R. Abeysekera, Structural properties of gelatin—Pectin gels. Part I: Effect of ethylene glycol. *Food Hydrocoll.* **11**, 271–279 (1997).
36. M. Yanagisawa, Y. Yamashita, S.-a. Mukai, M. Annaka, M. Tokita, Phase separation in binary polymer solution: Gelatin/Poly(ethylene glycol) system. *J. Mol. Liq.* **200**, 2–6 (2014).
37. J. L. Gornall, E. M. Terentjev, Helix–coil transition of gelatin: Helical morphology and stability. *Soft Matter* **4**, 544–549 (2008).
38. S. Sanwlani, P. Kumar, H. Bohidar, Hydration of gelatin molecules in glycerol–water solvent and phase diagram of gelatin organogels. *J. Phys. Chem. B* **115**, 7332–7340 (2011).
39. Y. Kim, X. Zhao, Magnetic soft materials and robots. *Chem. Rev.* **122**, 5317–5364 (2022).
40. M. Mebelli, D. Velliadou, M. J. Assael, M. L. Huber, Reference correlation for the viscosity of ethane-1,2-diol (ethylene glycol) from the triple point to 465 K and up to 100 MPa. *Int. J. Thermophys.* **42**, 10.1007/s10765-021-02867-0 (2021).

41. S. Akhtar, A. Omar Faruk, M. Saleh, Viscosity of aqueous solutions of formamide, *N*-methylformamide and *N*,*N*-dimethylformamide. *Phys. Chem. Liq.* **39**, 383–399 (2001).
42. J. Zielkiewicz, Excess molar volumes and excess Gibbs energies in *N*-methylformamide + water, or + methanol, or + ethanol at the temperature 303.15 K. *J. Chem. Eng. Data* **43**, 650–652 (1998).
43. K. V. Zaitseva, D. H. Zaitsau, M. A. Varfolomeev, S. P. Verevkin, Vapour pressures and enthalpies of vaporisation of alkyl formamides. *Fluid Ph. Equilib.* **494**, 228–238 (2019).
44. C. Tang, B. Du, S. Jiang, Z. Wang, X.-J. Liu, H. Zhao, A review on high-frequency dielectric elastomer actuators: Materials, dynamics, and applications. *Adv. Intell. Syst.* **6**, 2300047 (2024).
45. X. Huang, S. Zhang, P. Zhang, Y. Zhu, J. Xie, M. Yang, L. Han, J. Hu, Q. Li, J. He, Autonomous indication of electrical degradation in polymers. *Nat. Mater.* **23**, 237–243 (2024).
46. M. Yang, M. Guo, E. Xu, W. Ren, D. Wang, S. Li, S. Zhang, C.-W. Nan, Y. Shen, Polymer nanocomposite dielectrics for capacitive energy storage. *Nat. Nanotechnol.* **19**, 588–603 (2024).
47. S. Kim, Y.-H. Hsiao, Y. Lee, W. Zhu, Z. Ren, F. Niroui, Y. Chen, Laser-assisted failure recovery for dielectric elastomer actuators in aerial robots. *Sci. Robot.* **8**, eadf4278 (2023).
48. Y. Gao, X. Fang, D. Tran, K. Ju, B. Qian, J. Li, Dielectric elastomer actuators based on stretchable and self-healable hydrogel electrodes. *R. Soc. Open Sci.* **6**, 182145 (2019).
49. H. Wang, A. Gupta, Q. Lu, W. Wu, X. Wang, X. Huang, X. Hu, P. S. Lee, Ultrasoft and fast self-healing poly(ionic liquid) electrode for dielectric elastomer actuators. *Nat. Commun.* **16**, 7405 (2025).
50. F. Sun, Z. Li, S. Gao, Y. He, J. Luo, X. Zhao, D. Yang, T. Gao, H. Yang, P.-F. Cao, Self-healable, highly stretchable, ionic conducting polymers as efficient protecting layers for stable lithium-metal electrodes. *ACS Appl. Mater. Interfaces* **14**, 26014–26023 (2022).
51. Z. Peng, Y. Shi, N. Chen, Y. Li, Q. Pei, Stable and high-strain dielectric elastomer actuators based on a carbon nanotube-polymer bilayer electrode. *Adv. Funct. Mater.* **31**, 2008321 (2021).
52. H. Stoyanov, P. Brochu, X. Niu, C. Lai, S. Yun, Q. Pei, Long lifetime, fault-tolerant freestanding actuators based on a silicone dielectric elastomer and self-clearing carbon nanotube compliant electrodes. *RSC Adv.* **3**, 2272–2278 (2013).
53. W. Yuan, L. Hu, S. Ha, T. Lam, G. Grüner, Q. Pei, Self-clearable carbon nanotube electrodes for improved performance of dielectric elastomer actuators. *Proc. SPIE* **6927**, 69270P (2008).
54. Z. Peng, Y. Shi, Z. Xie, Y. Li, N. Chen, Q. Pei, Self-clearable bilayer electrode for dielectric elastomer actuators. *Proc. SPIE* **11587**, 115871Y (2021).
55. X. Zhao, Y. Zhou, Y. Song, J. Xu, J. Li, T. Tat, G. Chen, S. Li, J. Chen, Permanent fluidic magnets for liquid bioelectronics. *Nat. Mater.* **23**, 703–710 (2024).
56. M. Li, A. Pal, J. Byun, G. Gardi, M. Sitti, Magnetic putty as a reconfigurable, recyclable, and accessible soft robotic material. *Adv. Mater.* **35**, 2304825 (2023).
57. Y. Cheng, K. H. Chan, X.-Q. Wang, T. Ding, T. Li, C. Zhang, W. Lu, Y. Zhou, G. W. Ho, A fast autonomous healing magnetic elastomer for instantly recoverable, modularly programmable, and thermorecyclable soft robots. *Adv. Funct. Mater.* **31**, 2101825 (2021).
58. M. Sun, C. Tian, L. Mao, X. Meng, X. Shen, B. Hao, X. Wang, H. Xie, L. Zhang, Reconfigurable magnetic slime robot: Deformation, adaptability, and multifunction. *Adv. Funct. Mater.* **32**, 2112508 (2022).
59. Z. Chen, W. Lu, Y. Li, P. Liu, Y. Yang, L. Jiang, Solid–liquid state transformable magnetorheological millirobot. *ACS Appl. Mater. Interfaces* **14**, 30007–30020 (2022).
60. G. Dong, Q. He, S. Cai, Magnetic vitrimer-based soft robotics. *Soft Matter* **18**, 7604–7611 (2022).
61. Y. Lu, Z. Che, F. Sun, S. Chen, H. Zhou, P. Zhang, Y. Yu, L. Sheng, J. Liu, Mussel-inspired multifunctional integrated liquid metal-based magnetic suspensions with rheological, magnetic, electrical, and thermal reinforcement. *ACS Appl. Mater. Interfaces* **13**, 5256–5265 (2021).
62. H. Wei, B. Sun, S. Zhang, J. Tang, Magnetoactive millirobots with ternary phase transition. *ACS Appl. Mater. Interfaces* **16**, 3944–3954 (2024).

Acknowledgments

Funding: This work was supported by National Research Foundation of Korea (NRF) grants funded by Korean Government (RS-2024-00459269, NRF-RS-2021-NR059617, and 2018-052541). **Author contributions:** Y.H.L., S.W.M., and M.-G.L. conceived the concept and designed the experiments. Y.H.L. and S.W.M. fabricated the materials and devices and collected all data. H.-Y.K. and J.-Y.S. supervised the research. W.J.S., Y.E.C., G.S., J.C., B.I.P., and Y.L. provided advice on the main manuscript text. S.-Y.C. advised on the design of DEA devices. All authors contributed to data interpretation and manuscript preparation. Conceptualization: Y.H.L., S.W.M., M.-G.L., Y.L., H.-Y.K., and J.-Y.S. Methodology: Y.H.L., S.W.M., M.-G.L., W.J.S., H.-Y.K., and J.-Y.S. Investigation: Y.H.L., S.W.M., M.-G.L., and J.-Y.S. Visualization: Y.H.L., S.W.M., M.-G.L., W.J.S., S.-Y.C., G.S., Y.E.C., J.C., and J.-Y.S. Supervision: H.-Y.K. and J.-Y.S. Writing—original draft: Y.H.L., S.W.M., M.-G.L., Y.E.C., H.-Y.K., and J.-Y.S. Writing—review and editing: Y.H.L., S.W.M., M.-G.L., G.S., Y.E.C., J.C., B.I.P., H.-Y.K., and J.-Y.S. Software: Y.H.L., S.W.M., S.-Y.C., and J.-Y.S. Resources: J.-Y.S. Funding acquisition: H.-Y.K. and J.-Y.S. Data curation: Y.H.L., S.W.M., M.-G.L., and J.-Y.S. Validation: Y.H.L., S.W.M., M.-G.L., B.I.P., and J.-Y.S. Formal analysis: Y.H.L., S.W.M., M.-G.L., and J.-Y.S. Project administration: Y.H.L., S.W.M., M.-G.L., H.-Y.K., and J.-Y.S. **Competing interests:** The authors declare that they have no competing interests. **Data, code, and materials availability:** All data and code needed to evaluate and reproduce the results in the paper are present in the paper and/or the Supplementary Materials. All newly developed materials in this study are described in detail in Materials and Methods.

Submitted 25 August 2025
Accepted 13 February 2026
Published 20 March 2026
10.1126/sciadv.aeb7409

ScienceAdvances

A reconfigurable dielectric elastomer actuator via phase-transitional ferrofluid enables sustainable operation

Yun Hyeok Lee, Seung Won Moon, Min-Gyu Lee, Won Jun Song, Seong-Yu Choi, Gimin Sung, Yong Eun Cho, Junhyun Choi, Byung Ik Park, Younghoon Lee, Ho-Young Kim, and Jeong-Yun Sun

Sci. Adv. **12** (12), eaeb7409. DOI: 10.1126/sciadv.aeb7409

Science Advances
AAAS

Supplementary Materials for

A reconfigurable dielectric elastomer actuator via phase-transitional ferrofluid enables sustainable operation

Yun Hyeok Lee *et al.*

Corresponding author: Ho-Young Kim, hyk@snu.ac.kr; Jeong-Yun Sun, jysun@snu.ac.kr

Sci. Adv. **12**, eaeb7409 (2026)
DOI: 10.1126/sciadv.aeb7409

The PDF file includes:

Other Supplementary Material for this manuscript includes the following:

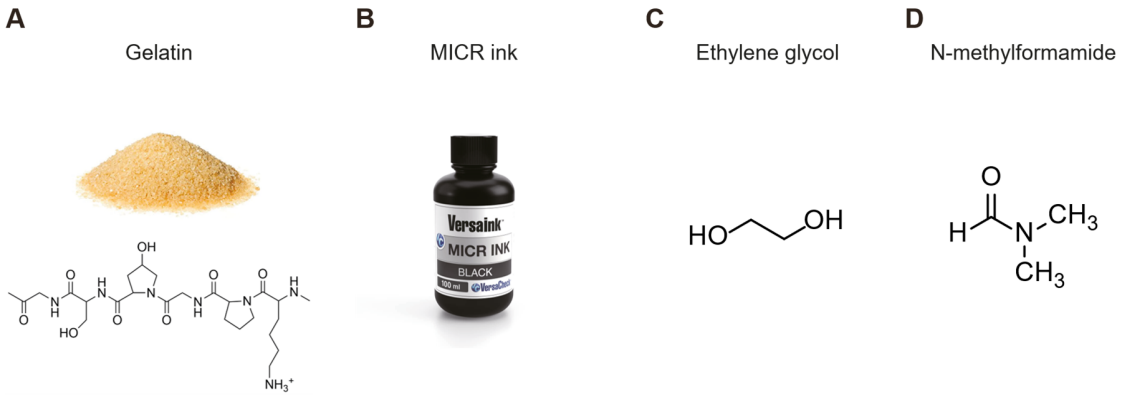

Fig. S1. Components of phase-transitional ferrofluid (PTF). (A) Gelatin as a phase-transitional polymer. **(B)** MICR (Magnetic Ink Character Recognition) ink as an aqueous ferrofluid. **(C)** Ethylene glycol (EG) as a solvent. **(D)** N-methylformamide (NMF) as a plasticizer.

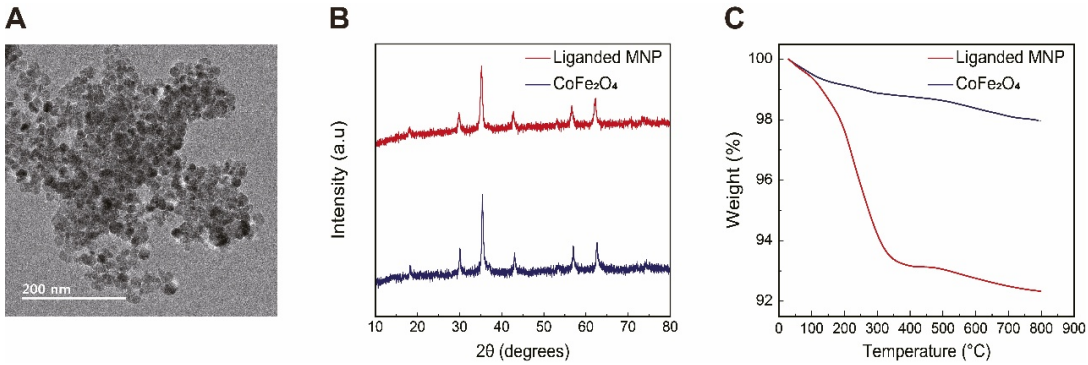

Fig. S2. Liganded MNP particle characteristics. (A) TEM image of liganded MNPs. **(B)** X-ray Diffraction (XRD) of liganded MNP and bare MNP. **(C)** Thermogravimetric Analysis (TGA) of liganded MNP and bare MNP.

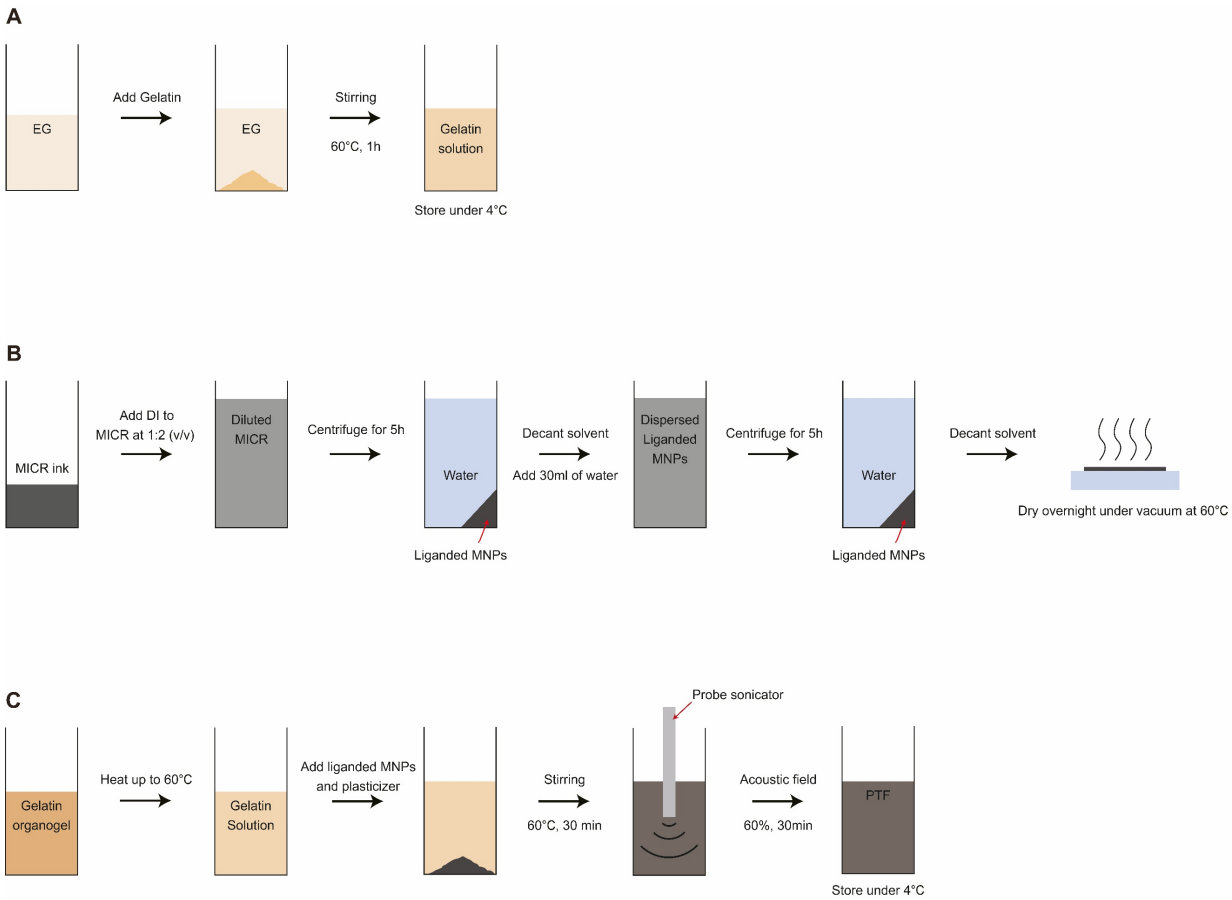

Fig. S3. Synthesis procedure of PTF. (A) Schematic illustration of preparing gelatin solution. **(B)** Schematic illustration of extracting MNPs out of MICR ink. **(C)** Schematic illustration of synthesizing PTF.

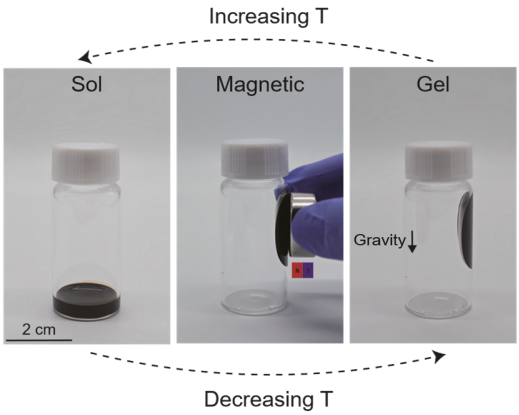

Fig. S4. Optical images of reversible phase transition system with magnetic responsibility.

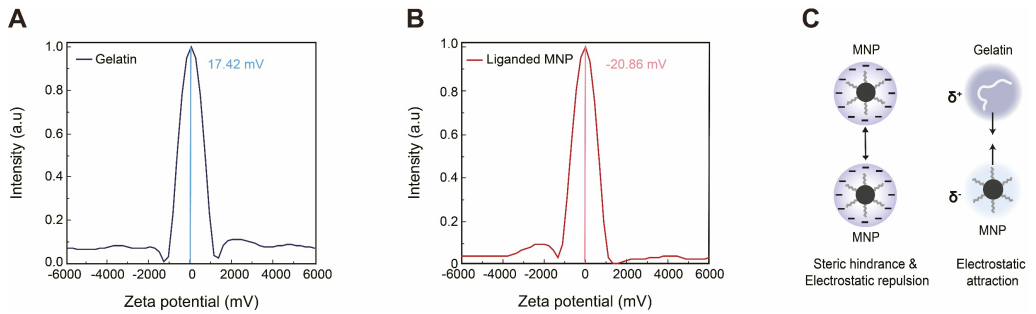

Fig. S5. Interactions between gelatin and liganded MNP. Zeta potential of **(A)** gelatin and **(B)** L-MNP in EG. **(C)** Steric hindrance and electrostatic repulsion among liganded MNPs, along with the electrostatic attraction between gelatin and liganded MNP, ensure a homogeneous system.

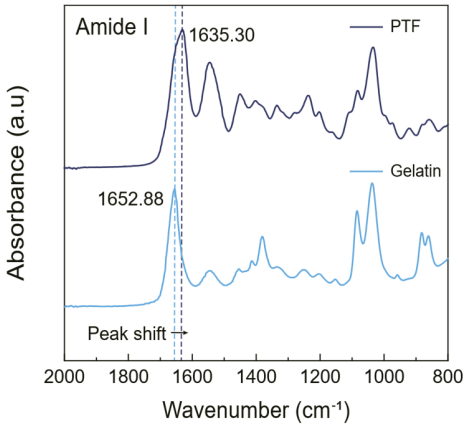

Fig. S6. FT-IR spectra of PTF and gelatin. The amide I stretching peak shift in PTF indicates interactions between liganded MNP and gelatin.

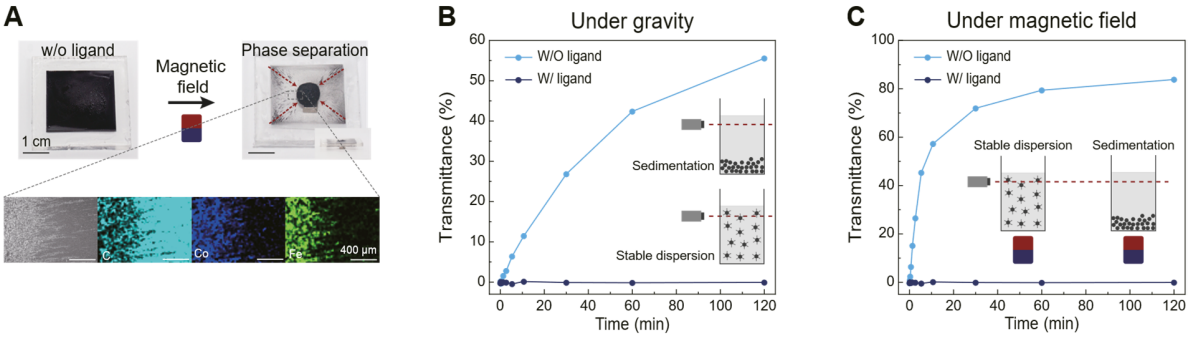

Fig. S7. Colloidal stability difference between liganded MNP and bare MNP based PTF. (A) Macroscopic behavior under magnetic field and corresponding SEM-EDS mapping of bare MNP based PTF. Transmittance vs. time of liganded MNP based PTF and bare MNP based PTF under **(B)** gravity and **(C)** magnetic field.

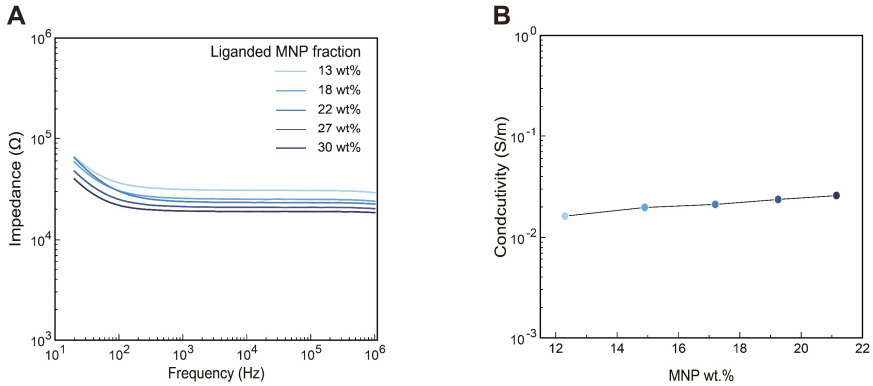

Fig. S8. Ionically conductive PTF. (A) Bode plot of PTF with varying MNP wt.%. **(B)** Conductivity of PTF with varying MNP wt.% at 1 MHz.

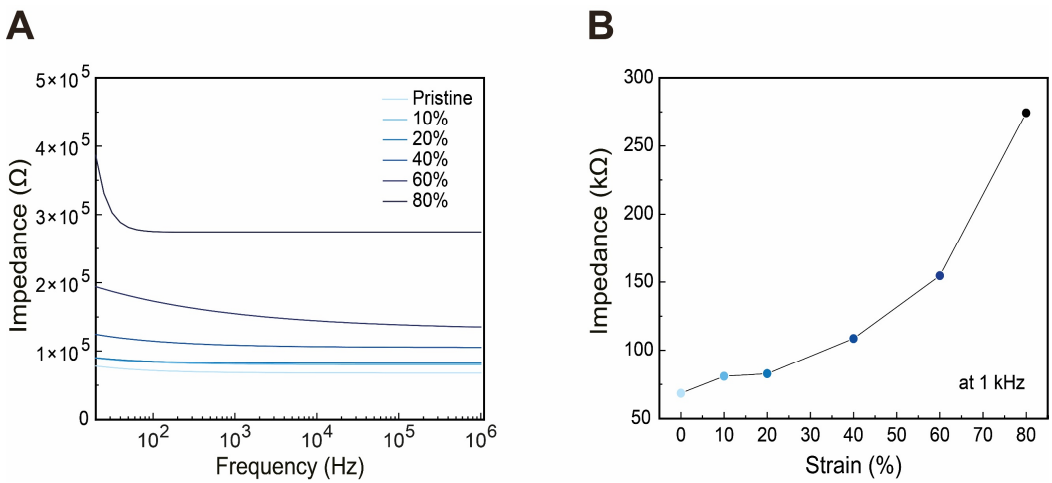

Fig. S9. Electrical properties of PTF as a stretchable electrode. (A) Impedance of PTF while stretching. **(B)** Impedance of PTF when they are stretched at 1 kHz.

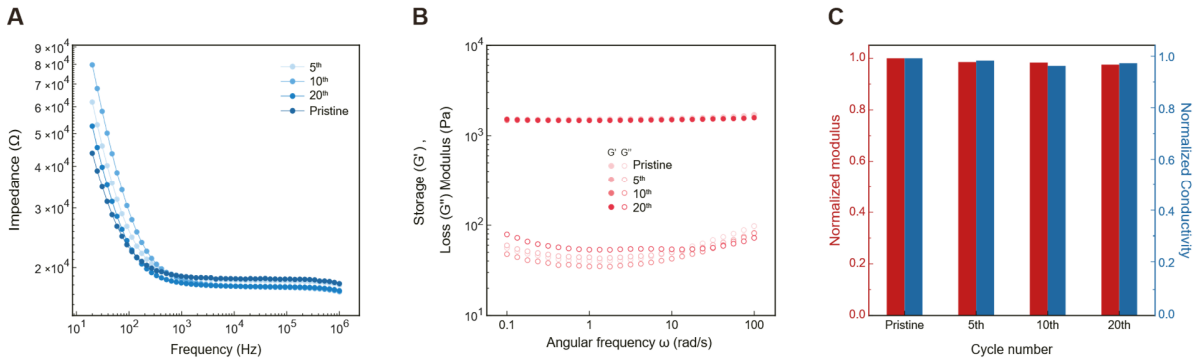

Fig. S10. Conductivity and rheological properties of PTF under repeated phase transition cycles. (A) Ionic conductivity of PTF after 0, 5, 10, and 20 phase transition cycles. **(B)** Rheological properties of PTF after 0, 5, 10, and 20 phase transition cycles. **(C)** Normalized conductivity and storage modulus with respect to the pristine sample after repeated phase transition cycles.

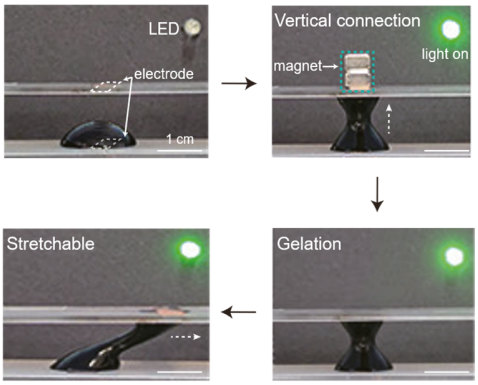

Fig. S11. Demonstration of PTF as a vertically connectable soft electrode.

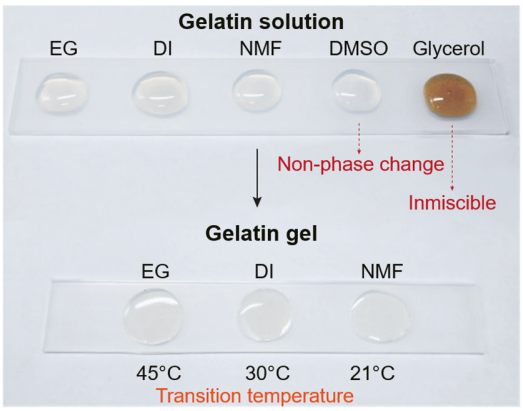

Fig. S12. Screening solvents compatible with gelatin.

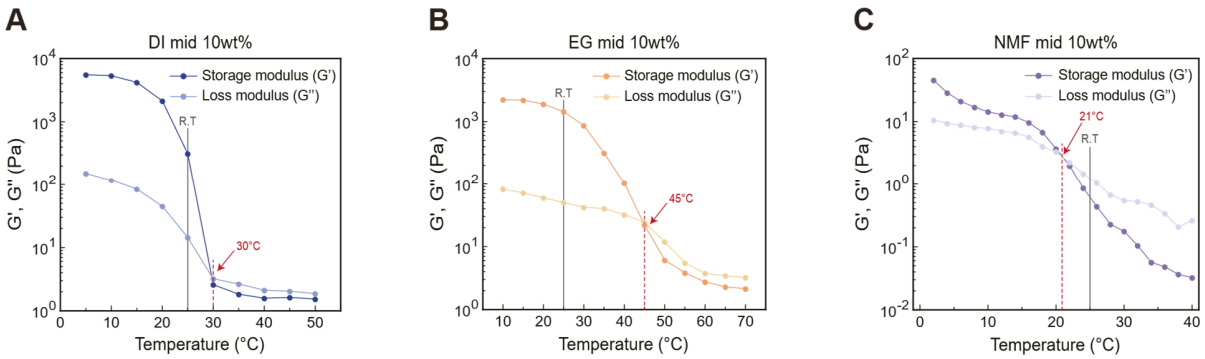

Fig. S13. Phase transition temperature of gelatin in various solvents. 10 wt.% of gelatin in **(A)** DI, **(B)** EG, and **(C)** NMF.

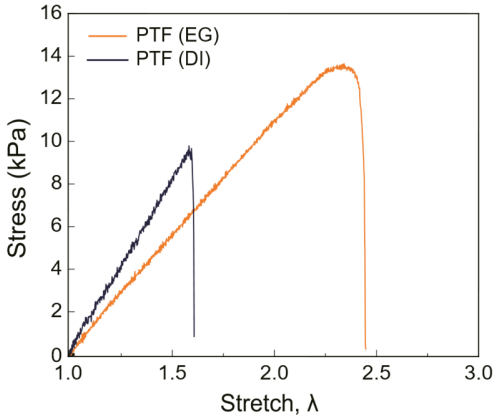

Fig. S14. Tensile test curves of EG-based and DI-based PTF.

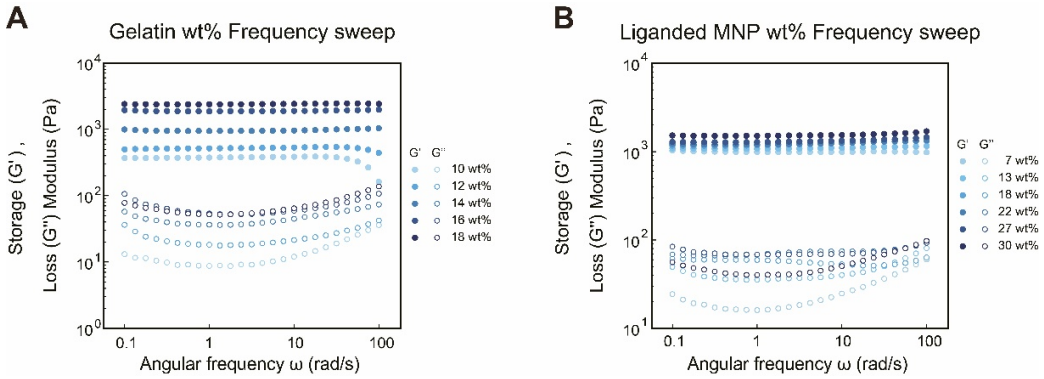

Fig. S15. Rheological properties of PTF with various gelatin and MNP contents. (A) Rheological frequency sweep with varying gelatin wt.%. **(B)** Rheological frequency sweep with varying MNP wt.%.

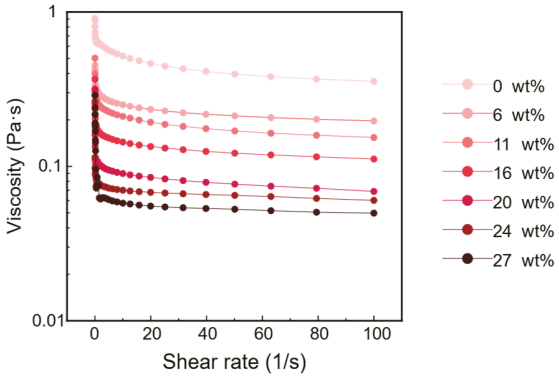

Fig. S16. Viscosity of PTF with varying NMF wt.%. The viscosity of PTF was measured by a rheological sweep test from 0.01 to 100 /s shear rate. Viscosity was defined as the plateau value.

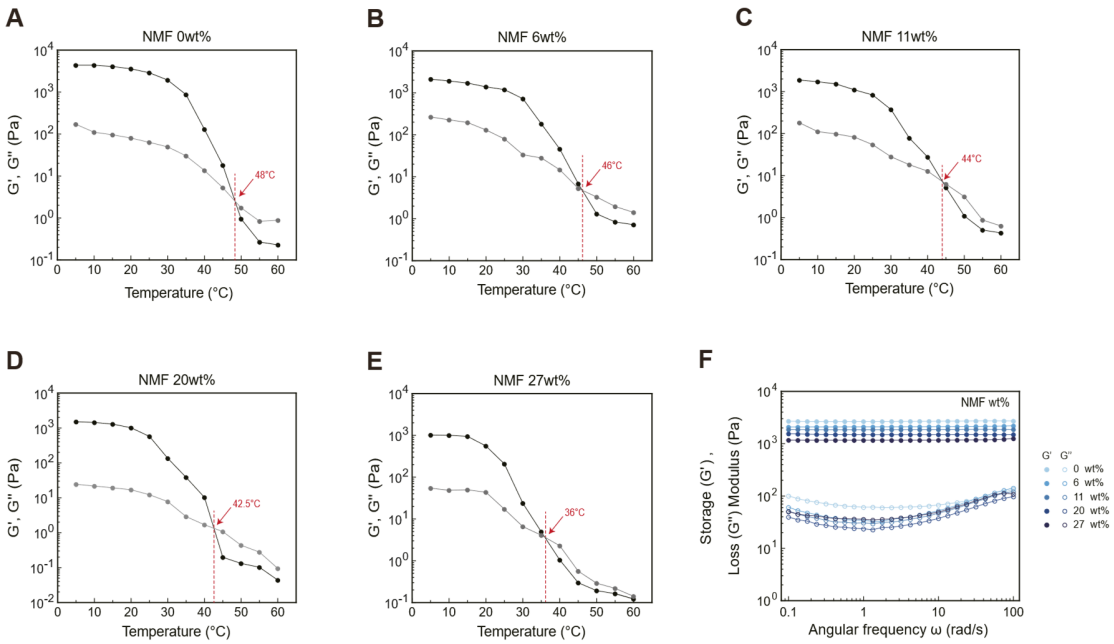

Fig. S17. Phase transition temperature of PTFs with varying plasticizer (NMF) contents and their rheological properties. Rheological temperature sweep data for samples containing plasticizers at **(A)** 0 wt.%, **(B)** 6 wt.%, **(C)** 11 wt.%, **(D)** 20 wt.%, and **(E)** 27 wt.%. **(F)** Rheological frequency sweep with varying plasticizer contents.

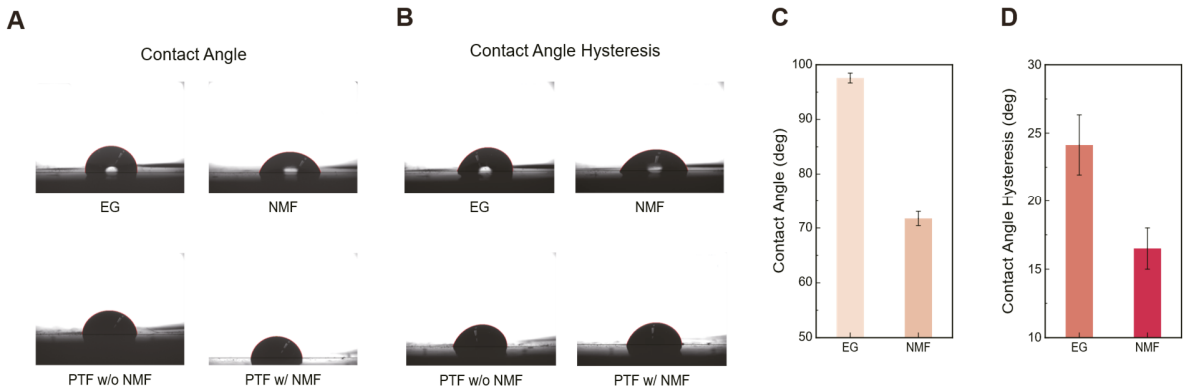

Fig. S18. Contact angle (CA) and Contact angle hysteresis (CAH) of EG, NMF, and PTF. Real images of the **(A)** CA and **(B)** CAH on Ecoflex surface of EG, NMF and PTF. **(C)** CA and **(D)** CAH of EG and NMF droplet on the Ecoflex surface.

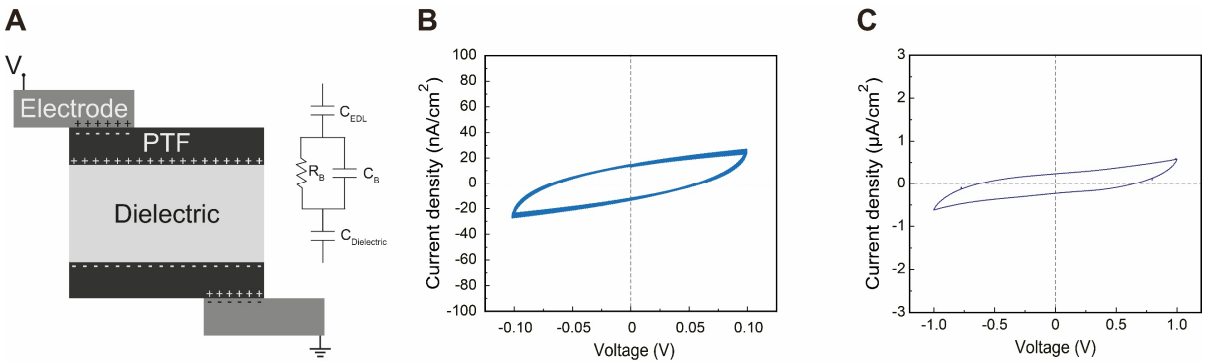

Fig. S19. DEA configuration and cyclic voltammetry of PTF. **(A)** DEA configuration and its equivalent circuit of PTF as an ionic conductor. **(B)** 7 cycles of cyclic voltammetry of PTF in range of -0.1 V to 0.1 V. Stable cycles show there are no electrochemical reaction in -0.1 V to 0.1 V. **(C)** Cyclic voltammetry of PTF in the range of -1 V to 1 V. There is no electrochemical reaction in the range of -1 V to 1 V.

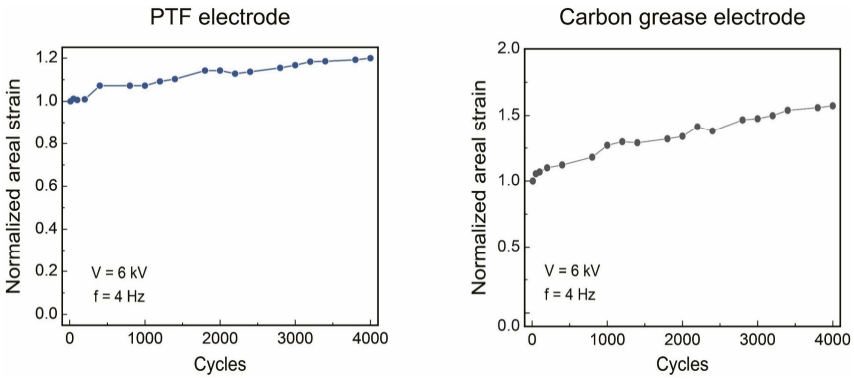

Fig. S20. Cyclic actuation test using PTF and carbon grease as the electrode for 4,000 cycles at 4 Hz.

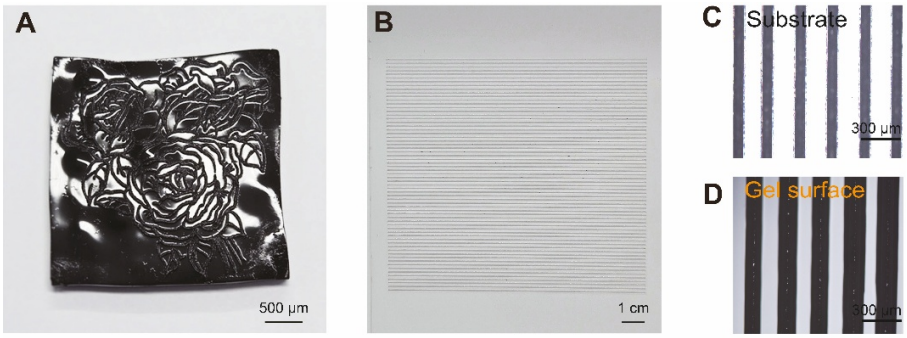

Fig. S21. Optical images of surface conformability of PTF by phase transition. (A) Optical image of PTF stripped from roses-engraved surface. **(B)** Optical image of surface for conformability test. **(C)** Magnified image of (B). **(D)** Optical image of stripped PTF surface from (B), exhibiting excellent surface conformability.

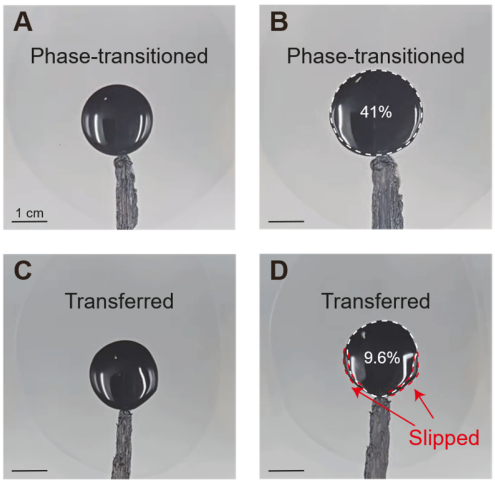

Fig. S22. | Images of phase-transitioned and transferred PTF during DEA actuation. (A) Phase-transitioned PTF at 0 MV/m. **(B)** Phase-transitioned PTF at 36 MV/m. **(C)** Transferred PTF at 0 MV/m. **(D)** Transferred PTF at 36 MV/m (slippage occurred). Ecoflex was used as a dielectric elastomer.

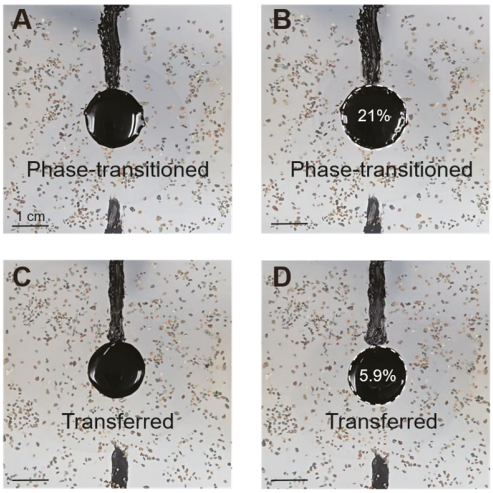

Fig. S23. Images of phase-transitioned and transferred PTF on a contaminated substrate during DEA actuation. (A) Phase-transitioned PTF at 0 MV/m. **(B)** Phase-transitioned PTF at 36 MV/m. **(C)** Transferred PTF at 0 MV/m. **(D)** Transferred PTF at 36 MV/m (slippage occurred). Ecoflex was used as a dielectric elastomer and natural sand particles (2.5 ~2.8 mm in diameter) were used as the contaminants.

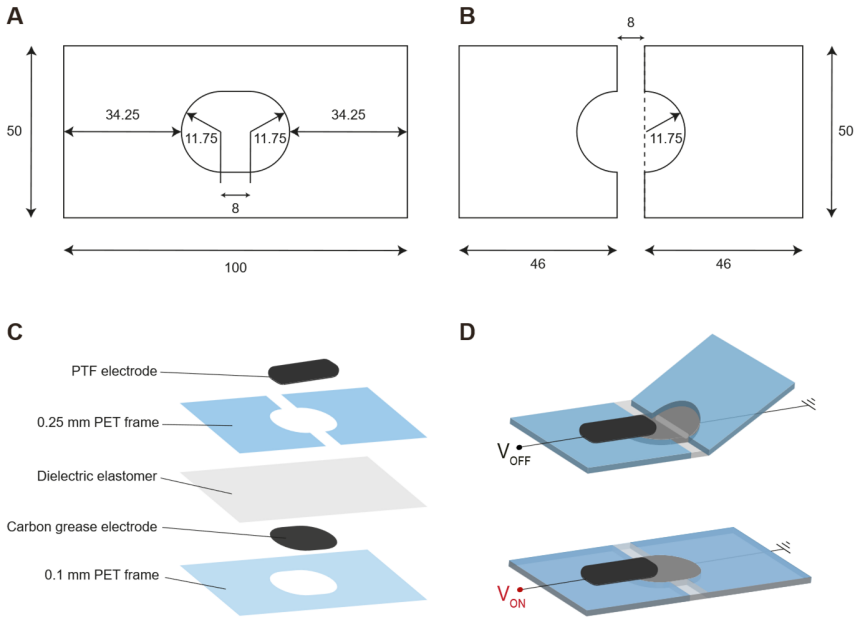

Fig. S24. Design of the bending actuator. (A) Dimensions of the 0.1 mm-thick PET frame. **(B)** Dimensions of the 0.25 mm-thick PET frame. (C) Multi-layered diagram of bending actuator. (D) Schematic of operating motion of the bending actuator.

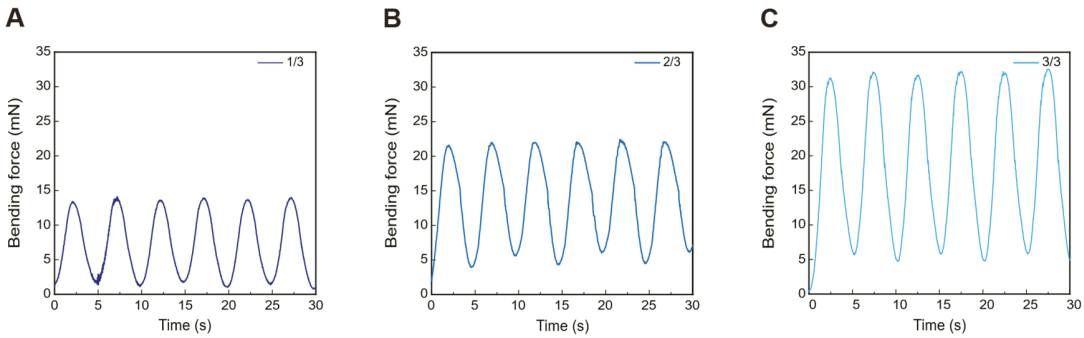

Fig. S25. Bending force of reconfigurable bending actuator. Bending force measured at three PTF overlapped position – **(A)** 1/3, **(B)** 2/3, and **(C)** fully (3/3) overlapped with the effective dielectric area of the bending actuator.

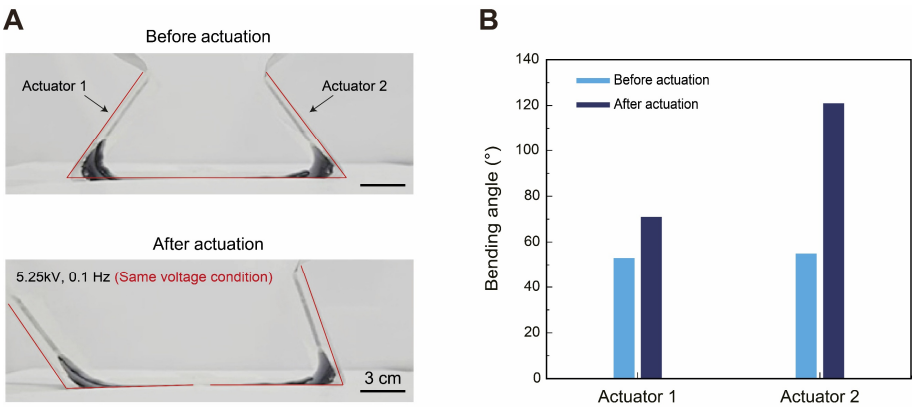

Fig. S26. Distinct actuation modes at the same voltage with reconfiguration. (A) Distinct actuator control enabled by reconfiguration with a single voltage source. **(B)** Bending angle of the actuators at the same voltage.

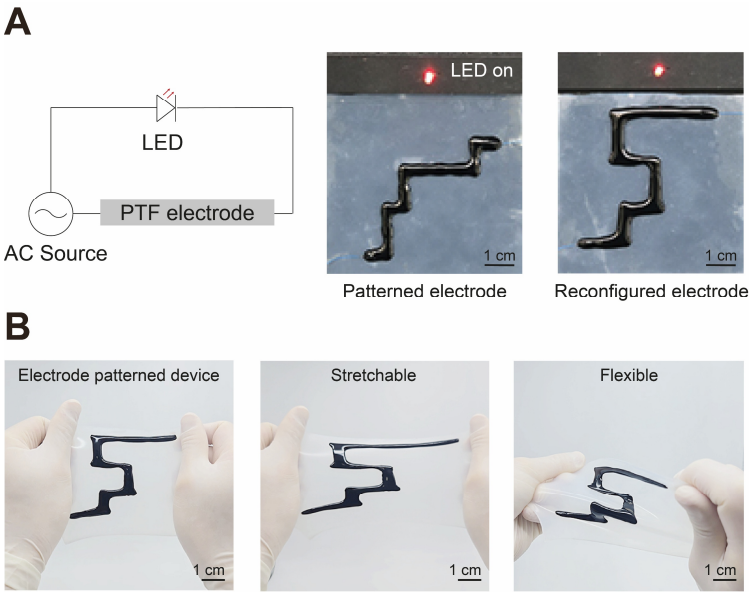

Fig. S27. Patterned circuit with PTF and its applications for stretchable devices. (A) Applications of PTF as an electrode for patterned circuit**. (B)** Application of PTF as an electrode for stretchable devices.

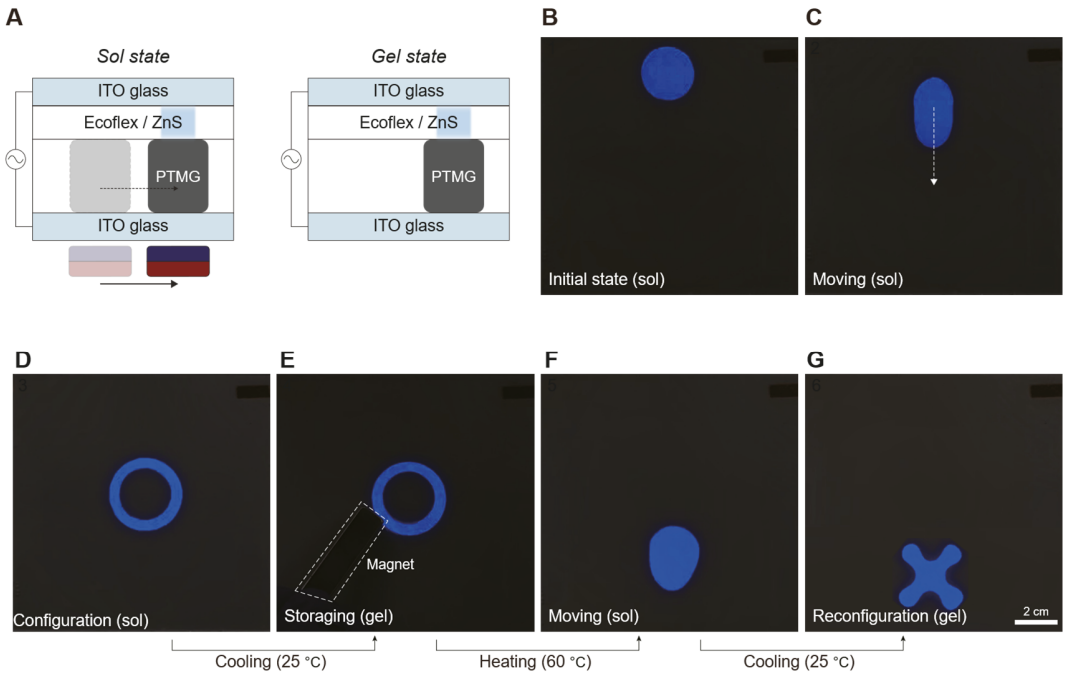

Fig. S28. PTF used for reconfigurable luminescent layer. (A) Schematics of reconfigurable luminescent layer. **(B)-(G)**, Process of reconfigurable luminescent layer operation. When an electric field is applied between the PTF and the ITO glass above, light is emitted from the luminescent layer containing ZnS particles. The movement of the sol-state PTF causes the location of the applied electric field to shift in real time. By inducing phase transition, the position of the PTF can be locked in place at a desired location. Once locked, the configuration remains stable even when an external electric field is applied. A subsequent phase transition can erase the existing optical memory and relock it at a new position in a different shape.

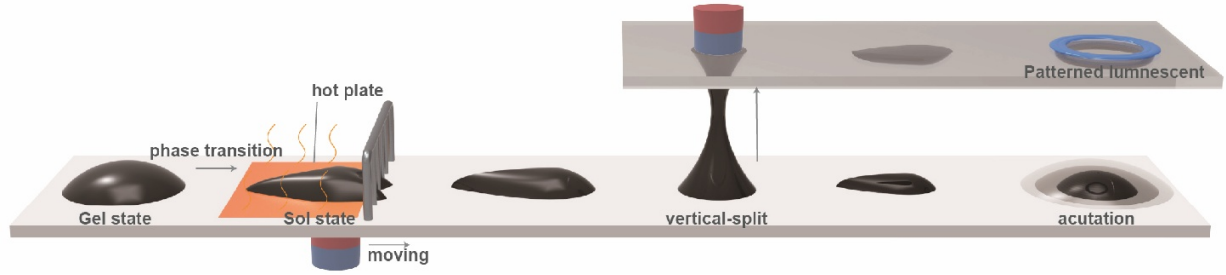

Fig. S29. PTF used for a three-dimensional integrated system.

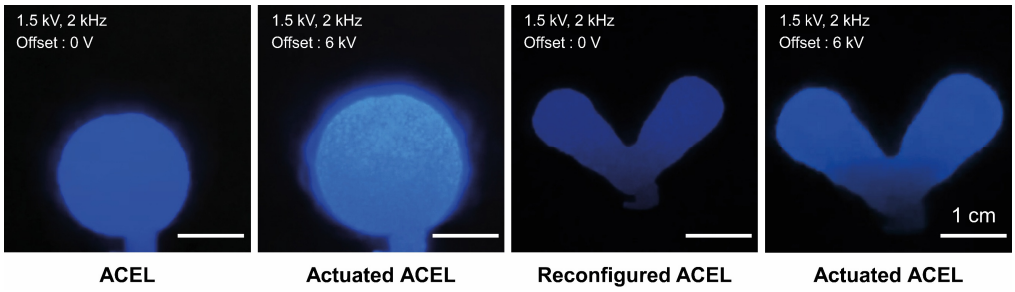

Fig. S30. DEA performance combined with ACEL.

Fig. S31. Recovery process of mechanically punctured DEA using PTF.

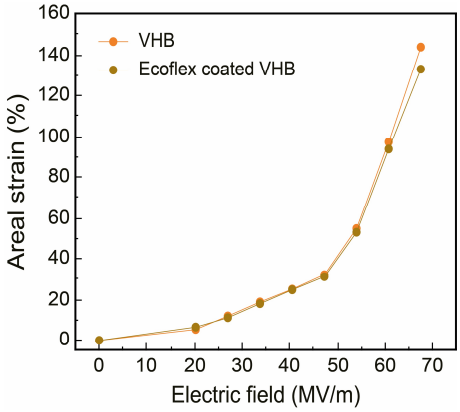

Fig. S32. DEA areal strain comparing bare VHB and Ecoflex coated VHB.

Types of magnetic system	Magnetic particles	Matrix components	tan δ	Viscosity (Pa·s)	Ref.
Reconfigurable magnetic soft systems	NdFeB (100 nm)	Magnetic chain network	1~7.273	4.5~7.5	(*55*)
	NdFeB (5 μm)	PDMS (Sylgard 184), boronic acid	1.4~2.5	30000~200000	(*56*)
	NdFeB	Alpha lipoic acid	0.818	9000	(*57*)
	NdFeB (5 μm)	PVA, sodium tetraborate	0.429	3.046	(*58*)
	Fe (10 μm)	Corn startch	0.367	350	(*59*)
	Fe_3O_4	Epoxy	0.2	200	(60)
	Fe	Liquid metal (EGaIn)	0.05~0.167	15~25	(61)
	Fe_3O_4	Gelatin (DI water)	0.075	1	(*62*)
Phase-transitional ferrofluid (PTF)	**$CoFe_2O_4$**	**Gelatin (Ethylene glycol, N-methylformamide)**	**0.03~0.05**	**0.06~0.1**	This work

Table S1. Comparison of elasticity (tan δ) and viscosity (η) in recent magnetically responsive soft materials.

Solvents	Solubility	Phase transition	B.P (°C)	M.P (°C)	Viscosity (mPa·s)	Vapor pressure (kPa)
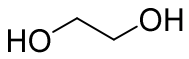 Ethylene glycol	O	O	195~198	-13	18.376 (20 °C)	0.011 (20 °C)
 DI water	O	O	100	0	1 (20 °C)	3.173 (25 °C)
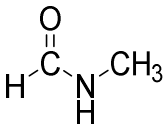 N-methylformamide	O	O	198~199	-4	1.68 (25 °C)	0.06 (25 °C)
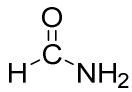 Formamide	O	X	210	2.6	3.76 (20 °C)	0.011 (20 °C)
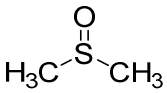 Dimethyl sulfoxide	O	X	189	16~19	2.14 (20 °C)	0.056 (20 °C)
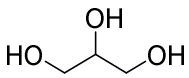 Glycerol	X	Δ	182	20	1412 (20 °C)	< 0.133 (20 °C)
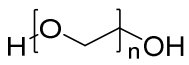 PEG 200	X	X	> 200 (degrade)	-65	50 (25 °C)	0.01 (20 °C)

Table S2. Solvent screening with Gelatin. We screened various solvents used with gelatin. Among them, EG, DI water, NMF, Formamide and DMSO were found to be miscible with gelatin as a single solvent. However, gelatin dissolved in DMSO and formamide did not undergo phase transition. Additionally, only gelatin dissolved in EG and DI water were able to maintain a stable gel state at room temperature.

Movie S1. Effect of ligands on magnetically driven collective motion in a sol state PTF.

To demonstrate the mediating role of ligands, ligand functionalized and bare MNP-based PTFs were compared by observing their sol state responses under a magnetic field. The former exhibits collective movement along the magnetic field (Fig. 1E). On the other hand, the latter shows phase separation of MNPs due to insufficient interactions among the MNPs, solvent, and polymers.

Movie S2. Soft and magneto-dynamic properties of PTF.

To demonstrate the magneto-dynamic motion of the PTF in its sol state, the material's response was examined while moving an external magnet. A high fraction of MNPs provided strong magnetic responsiveness, while plasticization lowered the viscosity, enabling highly dynamic motion under the magnetic field. In contrast, in the gel state the softness of the matrix preserved DEA performance, achieving 169% areal strain at 80 MV/m without compromising actuation.

Movie S3. Effect of phase transition rough surfaces on DEA performance.

To assess the impact of phase transition on interfacial conformability in DEAs, two configurations were compared: (i) PTF phase-transitioned in situ on the dielectric and (ii) PTF formed separately and transferred. Direct phase-transitioned PTF maintained robust surface adhesion (Fig. 3E and F), whereas transferred PTF exhibited interfacial slip once the applied voltage surpassed a critical level. This effect was further exacerbated when the interface was contaminated (Fig. 3G and H).

Movie S4. A reconfigurable dielectric elastomer actuator.

To exploit the magneto-dynamic and reversible phase-transitional capability of the PTF, a reconfigurable DEA with PTF electrode was demonstrated (Fig. 3I). From the initial actuation, the PTF can be phase-transitioned and relocated to other active sites to enable different actuation. Moreover, its fluidic nature allows splitting into multiple modules that can perform distinct actuation.

Movie S5. A reconfigurable bending actuator with tunable actuation.

To highlight the reconfigurable nature of PTF, the areal overlap between a PTF electrode and a bendable DEA was systematically varied (Fig. 3J). Increasing overlap enlarged the effective actuated area, producing greater bending angles (Fig. 3K).

Movie S6. A reconfigurable three dimensional electroactive systems.

To exhibit the versatility of the PTF electrode, a three-dimensional electroactive system was demonstrated. The liquid-like behavior of sol-state PTF allows navigation through complex obstacles and enables out-of-plane splitting, permitting electroluminescence and DEA actuation on separate planes along the z-axis simultaneously.

Movie S7. Self-healable PTF electrode for DEAs.

Through phase transition of the PTF, electrically disconnected electrode segments caused by damage can be rejoined under magnetic field guidance, enabling self-healing-induced recovery of the original actuation performance (Fig. 4D).

Movie S8. Sustainable DEA actuation in electrical failures.

In cases of electrical failures, the PTF electrode can isolate the defective site and restore functional actuation by magnetic reconfiguration, increasing the sustainability of DEAs (Fig. 4E).

Movie S9. Sustainable DEA actuation in mechanical failures.

In cases of mechanical failures with punctuation, the PTF electrode can isolate the defective site and restore its actuation by magnetic reconfiguration, increasing the sustainability of DEAs.

REFERENCES

1. Y. Lee, W. J. Song, J.-Y. Sun, Hydrogel soft robotics. *Mater. Today Phys.* **15**, 100258 (2020).

2. Y. Lee, W. J. Song, Y. Jung, H. Yoo, M.-Y. Kim, H.-Y. Kim, J.-Y. Sun, Ionic spiderwebs. *Sci. Robot.* **5**, eaaz5405 (2020).

3. J. Shintake, V. Cacucciolo, D. Floreano, H. Shea, Soft robotic grippers. *Adv. Mater.* **30**, 1707035 (2018).

4. W. J. Song, Y.-W. Kang, Y. H. Lee, J. Kim, B. F. G. Aymon, S.-Y. Choi, Y. E. Cho, X.-Y. Yan, S. Li, Y. Lee, X. Zhao, Y.-L. Park, J.-Y. Sun, All-3D-printed multi-environment modular microrobots powered by large-displacement dielectric elastomer microactuators. *Adv. Mater.* **37**, e07503 (2025).

5. C. S. Park, Y.-W. Kang, H. Na, J.-Y. Sun, Hydrogels for bioinspired soft robots. *Prog. Polym. Sci.* **150**, 101791 (2024).

6. V. Cacucciolo, J. Shintake, Y. Kuwajima, S. Maeda, D. Floreano, H. Shea, Stretchable pumps for soft machines. *Nature* **572**, 516–519 (2019).

7. T. J. Wallin, J. Pikul, R. F. Shepherd, 3D printing of soft robotic systems. *Nat. Rev. Mater.* **3**, 84–100 (2018).

8. C. Keplinger, J.-Y. Sun, C. C. Foo, P. Rothemund, G. M. Whitesides, Z. Suo, Stretchable, transparent, ionic conductors. *Science* **341**, 984–987 (2013).

9. D. Y. Kim, S. Choi, H. Cho, J.-Y. Sun, Electroactive soft photonic devices for the synesthetic perception of color and sound. *Adv. Mater.* **31**, e1804080 (2019).

10. E. Acome, S. K. Mitchell, T. Morrissey, M. Emmett, C. Benjamin, M. King, M. Radakovitz, C. Keplinger, Hydraulically amplified self-healing electrostatic actuators with muscle-like performance. *Science* **359**, 61–65 (2018).

11. X. Ji, X. Liu, V. Cacucciolo, M. Imboden, Y. Civet, A. El Haitami, S. Cantin, Y. Perriard, H. Shea, An autonomous untethered fast soft robotic insect driven by low-voltage dielectric elastomer actuators. *Sci. Robot.* **4**, eaaz6451 (2019).

12. Z. Suo, Theory of dielectric elastomers. *Acta Mech. Solida Sin.* **23**, 549–578 (2010).

13. X. Zhao, Z. Suo, Theory of dielectric elastomers capable of giant deformation of actuation. *Phys. Rev. Lett.* **104**, 178302 (2010).

14. G. Gu, J. Zou, R. Zhao, X. Zhao, X. Zhu, Soft wall-climbing robots. *Sci. Robot.* **3**, eaat2874 (2018).

15. Y. Chen, H. Zhao, J. Mao, P. Chirarattananon, E. F. Helbling, N.-S. P. Hyun, D. R. Clarke, R. J. Wood, Controlled flight of a microrobot powered by soft artificial muscles. *Nature* **575**, 324–329 (2019).

16. G. Sung, C. Yu, J.-M. Park, Y. H. Lee, C. S. Park, H. Lee, M. S. Kwon, J.-Y. Sun, High-k zwitterionic dielectric elastomers with internal plasticization for low-voltage actuation. *Mater. Today* **88**, 109–116 (2025).

17. J.-M. Park, C. S. Park, S. K. Kwak, J.-Y. Sun, Glass transition temperature as a unified parameter to design self-healable elastomers. *Sci. Adv.* **10**, eadp0729 (2024).

18. E. Hajiesmaili, D. R. Clarke, Dielectric elastomer actuators. *J. Appl. Phys.* **129**, 151102 (2021).

19. E. Hajiesmaili, N. M. Larson, J. A. Lewis, D. R. Clarke, Programmed shape-morphing into complex target shapes using architected dielectric elastomer actuators. *Sci. Adv.* **8**, eabn9198 (2022).

20. E. Hajiesmaili, D. R. Clarke, Reconfigurable shape-morphing dielectric elastomers using spatially varying electric fields. *Nat. Commun.* **10**, 183 (2019).

21. J. Wang, S. Li, D. Gao, J. Xiong, P. S. Lee, Reconfigurable and programmable origami dielectric elastomer actuators with 3D shape morphing and emissive architectures. *NPG Asia Mater.* **11**, 71 (2019).

22. H. Fu, Y. Jiang, J. Lv, Y. Huang, Z. Gai, Y. Liu, P. S. Lee, H. Xu, D. Wu, Multilayer dielectric elastomer with reconfigurable electrodes for artificial muscle. *Adv. Sci.* **10**, 2206094 (2023).

23. B. Aksoy, H. Shea, Reconfigurable and latchable shape-morphing dielectric elastomers based on local stiffness modulation. *Adv. Funct. Mater.* **30**, 2001597 (2020).

24. A. Chortos, J. Mao, J. Mueller, E. Hajiesmaili, J. A. Lewis, D. R. Clarke, Printing reconfigurable bundles of dielectric elastomer fibers. *Adv. Funct. Mater.* **31**, 2010643 (2021).

25. S. Rosset, H. R. Shea, Flexible and stretchable electrodes for dielectric elastomer actuators. *Appl. Phys. A* **110**, 281–307 (2013).

26. X. Fan, X. Dong, A. C. Karacakol, H. Xie, M. Sitti, Reconfigurable multifunctional ferrofluid droplet robots. *Proc. Natl. Acad. Sci. U.S.A.* **117**, 27916–27926 (2020).

27. X. Fan, Y. Jiang, M. Li, Y. Zhang, C. Tian, L. Mao, H. Xie, L. Sun, Z. Yang, M. Sitti, Scale-reconfigurable miniature ferrofluidic robots for negotiating sharply variable spaces. *Sci. Adv.* **8**, eabq1677 (2022).

28. W. Wang, J. V. Timonen, A. Carlson, D.-M. Drotlef, C. T. Zhang, S. Kolle, A. Grinthal, T.-S. Wong, B. Hatton, S. H. Kang, S. Kennedy, J. Chi, R. T. Blough, M. Sitti, L. Mahadevan, J. Aizenberg, Multifunctional ferrofluid-infused surfaces with reconfigurable multiscale topography. *Nature* **559**, 77–82 (2018).

29. M. Sun, S. Yang, J. Jiang, S. Jiang, M. Sitti, L. Zhang, Bioinspired self-assembled colloidal collectives drifting in three dimensions underwater. *Sci. Adv.* **9**, eadj4201 (2023).

30. M. Baumgartner, F. Hartmann, M. Drack, D. Preninger, D. Wirthl, R. Gerstmayr, L. Lehner, G. Mao, R. Pruckner, S. Demchyshyn, L. Reiter, M. Strobel, T. Stockinger, D. Schiller, S. Kimeswenger, F. Greibich, G. Buchberger, E. Bradt, S. Hild, S. Bauer, M. Kaltenbrunner,

Resilient yet entirely degradable gelatin-based biogels for soft robots and electronics. *Nat. Mater.* **19**, 1102–1109 (2020).

31. T. Li, H. Qi, C. Zhao, Z. Li, W. Zhou, G. Li, H. Zhuo, W. Zhai, Robust skin-integrated conductive biogel for high-fidelity detection under mechanical stress. *Nat. Commun.* **16**, 88 (2025).

32. Y. H. Lee, W. J. Song, J.-M. Park, G. Sung, M.-G. Lee, M. Kim, S. Park, J. S. Lee, M. Kim, W. S. Kim, J.-Y. Sun, Full-color generation via phototunable mono ink for fast and elaborate printings. *Adv. Mater.* **35**, e2307165 (2023).

33. F. Gao, H. Jiang, D. Wang, S. Wang, W. Song, Bio-inspired magnetic-responsive supramolecular-covalent semi-convertible hydrogel. *Adv. Mater.* **36**, 2401645 (2024).

34. H. Yoo, Y. H. Lee, M.-G. Lee, J.-Y. Sun, Gel-based ionic circuits. *Chem. Rev.* **125**, 8956–9011 (2025).

35. I. S. Chronakis, S. Kasapis, R. Abeysekera, Structural properties of gelatin—Pectin gels. Part I: Effect of ethylene glycol. *Food Hydrocoll.* **11**, 271–279 (1997).

36. M. Yanagisawa, Y. Yamashita, S.-a. Mukai, M. Annaka, M. Tokita, Phase separation in binary polymer solution: Gelatin/Poly(ethylene glycol) system. *J. Mol. Liq.* **200**, 2–6 (2014).

37. J. L. Gornall, E. M. Terentjev, Helix–coil transition of gelatin: Helical morphology and stability. *Soft Matter* **4**, 544–549 (2008).

38. S. Sanwlani, P. Kumar, H. Bohidar, Hydration of gelatin molecules in glycerol–water solvent and phase diagram of gelatin organogels. *J. Phys. Chem. B* **115**, 7332–7340 (2011).

39. Y. Kim, X. Zhao, Magnetic soft materials and robots. *Chem. Rev.* **122**, 5317–5364 (2022).

40. M. Mebelli, D. Velliadou, M. J. Assael, M. L. Huber, Reference correlation for the viscosity of ethane-1,2-diol (ethylene glycol) from the triple point to 465 K and up to 100 MPa. *Int. J. Thermophys.* **42**, 10.1007/s10765-021-02867-0 (2021).

41. S. Akhtar, *A. Omar* Faruk, M. Saleh, Viscosity of aqueous solutions of formamide, *N*-methylformamide and *N*,*N*-dimethylformamide. *Phys. Chem. Liq.* **39**, 383–399 (2001).

42. J. Zielkiewicz, Excess molar volumes and excess Gibbs energies in *N*-methylformamide + water, or + methanol, or + ethanol at the temperature 303.15 K. *J. Chem. Eng. Data* **43**, 650–652 (1998).

43. K. V. Zaitseva, D. H. Zaitsau, M. A. Varfolomeev, S. P. Verevkin, Vapour pressures and enthalpies of vaporisation of alkyl formamides. *Fluid Ph. Equilib.* **494**, 228–238 (2019).

44. C. Tang, B. Du, S. Jiang, Z. Wang, X.-J. Liu, H. Zhao, A review on high-frequency dielectric elastomer actuators: Materials, dynamics, and applications. *Adv. Intell. Syst.* **6**, 2300047 (2024).

45. X. Huang, S. Zhang, P. Zhang, Y. Zhu, J. Xie, M. Yang, L. Han, J. Hu, Q. Li, J. He, Autonomous indication of electrical degradation in polymers. *Nat. Mater.* **23**, 237–243 (2024).

46. M. Yang, M. Guo, E. Xu, W. Ren, D. Wang, S. Li, S. Zhang, C.-W. Nan, Y. Shen, Polymer nanocomposite dielectrics for capacitive energy storage. *Nat. Nanotechnol.* **19**, 588–603 (2024).

47. S. Kim, Y.-H. Hsiao, Y. Lee, W. Zhu, Z. Ren, F. Niroui, Y. Chen, Laser-assisted failure recovery for dielectric elastomer actuators in aerial robots. *Sci. Robot.* **8**, eadf4278 (2023).

48. Y. Gao, X. Fang, D. Tran, K. Ju, B. Qian, J. Li, Dielectric elastomer actuators based on stretchable and self-healable hydrogel electrodes. *R. Soc. Open Sci.* **6**, 182145 (2019).

49. H. Wang, A. Gupta, Q. Lu, W. Wu, X. Wang, X. Huang, X. Hu, P. S. Lee, Ultrasoft and fast self-healing poly(ionic liquid) electrode for dielectric elastomer actuators. *Nat. Commun.* **16**, 7405 (2025).

50. F. Sun, Z. Li, S. Gao, Y. He, J. Luo, X. Zhao, D. Yang, T. Gao, H. Yang, P.-F. Cao, Self-healable, highly stretchable, ionic conducting polymers as efficient protecting layers for stable lithium-metal electrodes. *ACS Appl. Mater. Interfaces* **14**, 26014–26023 (2022).

51. Z. Peng, Y. Shi, N. Chen, Y. Li, Q. Pei, Stable and high-strain dielectric elastomer actuators based on a carbon nanotube-polymer bilayer electrode. *Adv. Funct. Mater.* **31**, 2008321 (2021).

52. H. Stoyanov, P. Brochu, X. Niu, C. Lai, S. Yun, Q. Pei, Long lifetime, fault-tolerant freestanding actuators based on a silicone dielectric elastomer and self-clearing carbon nanotube compliant electrodes. *RSC Adv.* **3**, 2272–2278 (2013).

53. W. Yuan, L. Hu, S. Ha, T. Lam, G. Grüner, Q. Pei, Self-clearable carbon nanotube electrodes for improved performance of dielectric elastomer actuators. *Proc. SPIE* **6927**, 69270P (2008).

54. Z. Peng, Y. Shi, Z. Xie, Y. Li, N. Chen, Q. Pei, Self-clearable bilayer electrode for dielectric elastomer actuators. *Proc. SPIE* **11587**, 115871Y (2021).

55. X. Zhao, Y. Zhou, Y. Song, J. Xu, J. Li, T. Tat, G. Chen, S. Li, J. Chen, Permanent fluidic magnets for liquid bioelectronics. *Nat. Mater.* **23**, 703–710 (2024).

56. M. Li, A. Pal, J. Byun, G. Gardi, M. Sitti, Magnetic putty as a reconfigurable, recyclable, and accessible soft robotic material. *Adv. Mater.* **35**, 2304825 (2023).

57. Y. Cheng, K. H. Chan, X.-Q. Wang, T. Ding, T. Li, C. Zhang, W. Lu, Y. Zhou, G. W. Ho, A fast autonomous healing magnetic elastomer for instantly recoverable, modularly programmable, and thermorecyclable soft robots. *Adv. Funct. Mater.* **31**, 2101825 (2021).

58. M. Sun, C. Tian, L. Mao, X. Meng, X. Shen, B. Hao, X. Wang, H. Xie, L. Zhang, Reconfigurable magnetic slime robot: Deformation, adaptability, and multifunction. *Adv. Funct. Mater.* **32**, 2112508 (2022).

59. Z. Chen, W. Lu, Y. Li, P. Liu, Y. Yang, L. Jiang, Solid–liquid state transformable magnetorheological millirobot. *ACS Appl. Mater. Interfaces* **14**, 30007–30020 (2022).

60. G. Dong, Q. He, S. Cai, Magnetic vitrimer-based soft robotics. *Soft Matter* **18**, 7604–7611 (2022).

61. Y. Lu, Z. Che, F. Sun, S. Chen, H. Zhou, P. Zhang, Y. Yu, L. Sheng, J. Liu, Mussel-inspired multifunctional integrated liquid metal-based magnetic suspensions with rheological, magnetic, electrical, and thermal reinforcement. *ACS Appl. Mater. Interfaces* **13**, 5256–5265 (2021).

62. H. Wei, B. Sun, S. Zhang, J. Tang, Magnetoactive millirobots with ternary phase transition. *ACS Appl. Mater. Interfaces* **16**, 3944–3954 (2024).